Acta Biomaterialia 185 (2024) 266–280

Contents lists available at ScienceDirect

Acta Biomaterialia

journal homepage: www.elsevier.com/locate/actbio

Full length article

Second harmonic generation microscopy, biaxial mechanical tests and fiber dispersion models in human skin biomechanics

Riccardo Alberini[a], Andrea Spagnoli[a,*], Mohammad Javad Sadeghinia[b], Bjorn Skallerud[b], Michele Terzano[c], Gerhard A. Holzapfel[b,c]

[a] Department of Engineering and Architecture, University of Parma, Parma, Italy
[b] Department of Structural Engineering, Norwegian University of Science and Technology (NTNU), Trondheim, Norway
[c] Institute of Biomechanics, Graz University of Technology, Graz, Austria

ARTICLE INFO

Article history:
Received 27 February 2024
Revised 13 July 2024
Accepted 16 July 2024
Available online 22 July 2024

Keywords:
Second harmonic generation
Planar biaxial test
Human skin
Collagen fibers
Hyperelasticity
Microstructure modeling
Fiber dispersion models

ABSTRACT

Advanced numerical simulations of the mechanical behavior of human skin require thorough calibration of the material's constitutive models based on experimental *ex vivo* mechanical tests along with images of tissue microstructure for a variety of biomedical applications. In this work, a total of 14 human healthy skin samples and 4 additional scarred skin samples were experimentally analyzed to gain deep insights into the biomechanics of human skin. In particular, second harmonic generation (SHG) microscopy was used to extract detailed images of the distribution of collagen fibers, which were subsequently processed using a three-dimensional Fourier transform-based method recently proposed by the authors to quantify the distribution of fiber orientations. Mechanical tests under both biaxial and uniaxial loading were performed to calibrate the relevant mechanical parameters of two widely used constitutive models of soft fiber-reinforced biological tissues that account for non-symmetrical fiber dispersion. The calibration of the models allowed us to identify correlations between the mechanical parameters of the constitutive models considered.

Statement of significance

Constitutive models for soft collagenous tissues can accurately reproduce the complex nonlinear and anisotropic mechanical behavior of skin. However, a comprehensive analysis of both microstructural and mechanical parameters is still missing for human skin. In this study, these parameters are determined by combining biaxial mechanical tests and SHG stacks of collagen fibers on ex vivo healthy human skin samples. The constitutive parameters are provided for two widely used hyperelastic models and enable accurate characterization of skin mechanical behavior for advanced numerical simulations.

1. Introduction

The skin is the largest organ in the human body, accounting for 15% of the total body weight [1], and serves as a primary barrier against various external hazards such as bacterial attack, physical harm and sun exposure [2]. At the same time, the skin carries out several biological activities, including D-vitamin synthesis, energy storage, and thermoregulation [3]. Due to constant exposure to external threats, the skin exhibits a complex mechanical behavior that ensures the integrity of the tissue required to preserve its vital functions. The dermis lies between the outermost epidermis and the deeper hypodermis layers and is the main layer responsible for the mechanical strength of the skin. It has an extracellular matrix consisting of a dense network of wavy collagen fibers (60–80%of dry weight) and elastin fibers (1–4% of dry weight) [4,5] embedded in a semi-fluid substance of proteoglycans (~ 20% of dry weight), known as ground substance [6]. Due to this microstructural composition, the overall mechanical behavior of the skin is highly nonlinear and characterized by a pronounced J-shaped loading curve [7]. During the initial loading phase, the waviness of the collagen fibers allows for significant deformation under relatively low applied loads. In this phase the mechanical response is con-

* Corresponding author.
E-mail address: spagnoli@unipr.it (A. Spagnoli).

https://doi.org/10.1016/j.actbio.2024.07.026

trolled by the ground substance and the elastin fibers, the latter also being responsible for the recoil mechanism of the collagen fibers during unloading [8–10]. Then, as the deformation increases, the collagen fibers become more and more straightened in the direction of the load, ultimately reaching an almost linear phase with a significantly higher stiffness [11,12]. Due to the non-uniform orientation distribution of the collagen fibers, the response is also anisotropic [7,13]. In particular, the mean orientation of the fibers and the degree of their dispersion is not the same throughout the body, but varies depending on the anatomical region. The map of these fiber directions is represented by the well-known Langer's lines [14]. In addition, the mechanical properties of the skin are different in each person and are influenced by several biological factors, including age, sex, location on the body and pathologies [15–18]. For example, collagen density reduces with age, thus reducing the stiffness in the final linear region and the maximum tensile stress [19].

The intricate connection between these properties and the tissue microstructure has garnered considerable theoretical interest. In fact, modeling such a behavior is of great interest for medical and engineering purposes, including the development of drug delivery systems [20–22], the optimization of skin correction surgeries [23,24], the analysis of skin-orthopedic tape interactions [25], and the development of stretchable electronics [26,27] and soft robotics [28,29].

There are several constitutive models in the literature to describe the mechanical behavior of soft collagenous tissues such as skin, each with advantages and disadvantages. In particular, structure-based constitutive models use microstructural parameters to describe the anisotropy resulting from the non-uniform orientation distribution of collagen fibers and mechanical parameters to capture the strong nonlinearity. One of the most popular is the Generalized Structure Tensor (GST) model proposed by Holzapfel et al. [30]. For example, this model has been calibrated for an abdominal aortic aneurysm [31], corneal tissue [32], and mitral valve leaflets [33]. Another valuable approach has been proposed by Li et al. [34], who developed the discrete fiber dispersion (DFD) model as an alternative to the GST model to account for the non-compressive behavior of collagen fibers using a computationally efficient formulation.

To calibrate these models for the skin, either *in vivo* or *ex vivo* tests can be performed. While microstructural parameters can be derived from second harmonic generation (SHG) images of collagen fibers using automated algorithms [31,35], mechanical parameters must be obtained through mechanical tests. *In vivo* tests have been extensively used in the literature to characterize the mechanical behavior of the skin, with techniques based on suction [36,37], indentation [38,39] and wave propagation [40,41], to name just a few. These methods have the advantage of providing information about the skin in its natural state, but are affected by several uncertainties regarding pre-stress and boundary conditions [5]. In addition, due to the non-invasive and non-destructive nature of *in vivo* tests, the range of investigated deformations is constrained to the range of physiological strains and therefore limits the information required for accurate constitutive modeling [5]. On the other hand, *ex vivo* experiments on representative skin samples can characterize the mechanical response over a full range of deformations. The current standard for investigating soft tissues properties is the biaxial tensile test [42]. In contrast to uniaxial testing, skin samples are loaded in two perpendicular directions simultaneously. Since the applied deformation can be controlled independently for both directions, different loading protocols can be performed, providing the necessary mechanical data to define the material parameters for anisotropic models [43,44]. Biaxial testing has been widely employed to determine the mechanical parameters for several tissues, such as aortic walls [31] and mitral valve leaflets [33,45].

Despite its importance, there are relatively few studies calibrating structure-based mechanical models for the human skin using *ex vivo* tests. For example, Ní Annaidh et al. [46] investigated both mechanical and microstructural parameters of *ex vivo* samples using uniaxial tests along different directions relative to the Langer's lines, but provided limited mechanical data for model fitting. Other relevant studies by Tonge et al. [47] and Diab et al. [48] applied inflation tests to obtain biaxial mechanical data, but then obtained microstructural parameters through mechanical fitting rather than from images of the fiber microstructure, thereby reducing the physical significance of their results. More recently, Meador et al. [49] has thoroughly analyzed mouse skin, including biaxial testing and microstructural investigations, as well as considering the effects of physiological pre-strain on mechanical parameters. To date, no comparable comprehensive study has been conducted on human skin that included both biaxial tests and microstructural analysis.

To close this gap, the results of an experimental campaign on human skin samples are presented here. Fourteen healthy samples from the lower abdominal region were tested to obtain the mechanical and microstructural parameters for the GST and DFD models, the first representing a standard for modeling soft fibrous tissues and the second having high potential for advanced simulations [50]. In particular, microstructural parameters describing the full three-dimensional fiber dispersion were derived for the first time using an algorithm based on the 3D discrete Fourier transform algorithm proposed by Alberini et al. [51]. Uniaxial tests were also performed to investigate the volumetric change of the skin in the uniaxial region, suggesting some limits to the generally accepted assumption of incompressibility. In addition, four samples derived from a scar tissue were analyzed to observe the microstructural differences compared to healthy skin.

2. Methods

2.1. Tissue acquisition and storage

Human skin samples were obtained from the surplus tissue of routine abdominal skin reduction surgeries at St. Olavs University Hospital, Trondheim, and at the private hospital Aleris Solsiden, Trondheim. All the patients provided written informed consent prior the surgical intervention. The study was approved by the Regional Committee for Medical and Health Research Ethics (Project ID: 474249), and all examinations were performed in accordance with the rules for the investigation of human subjects set out in the Declaration of Helsinki.

Fourteen square-shape samples of about 20 mm × 20 mm and close to the sagittal plane were obtained from the left and right sides of 3 patients. Patient 1, female, 67 years old, 6 samples; Patient 2, female, 40, 4 samples; Patient 3, male, 20, 4 samples. Four additional samples were collected from an old Cesarean section scar of Patient 2, of which 2 contained healthy tissue and 2 contained scar tissue. After excision, the x and y axes were recorded on the epidermis with a permanent marker and the excess adipose tissue was removed, leaving only a layer of about 1 mm. The x axis coincided with the frontal (horizontal) axis for the fourteen healthy samples, while it was taken aligned with the scar axis in the other four samples. The samples were then stored at −28 °C prior to testing, within 2 h of harvest.

2.2. Planar tensile tests

To prepare the samples for the mechanical tests, the remaining layer of adipose tissue was carefully removed while still frozen, ensuring that the dermis was not damaged during this process. Samples were then trimmed to an approximate size of 15 mm × 15 mm,

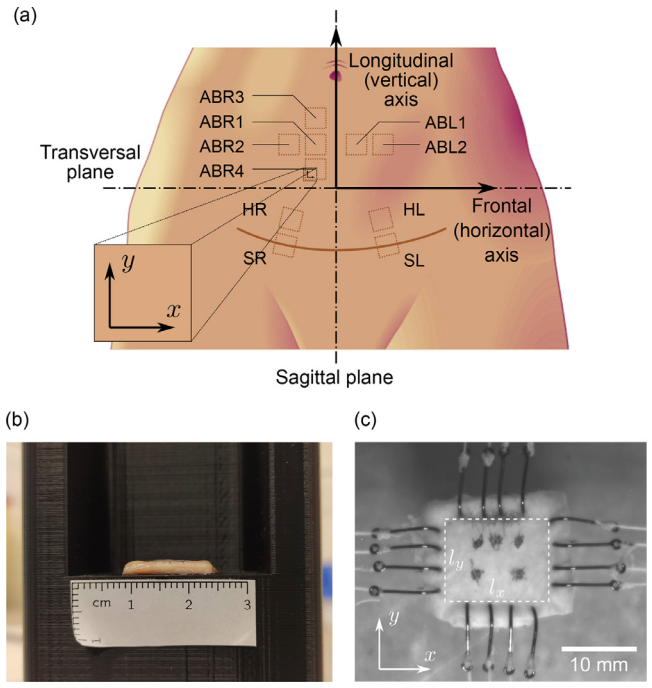

Fig. 1. Location of samples and views of a representative sample: (a) schematic representation of the approximate location (not to scale) and nomenclature of the samples. In the lower left corner of each sample, the corresponding x and y axes are shown; (b) side view of the sample ABR3-p1 used for thickness measurement; (c) top view of the same sample mounted on the biaxial machine, with a dashed line highlighting the effectively tested sample area enclosed by the hooks with horizontal and vertical sizes l_x and l_y, respectively. The four fiducial markers at the corners are used to compute the deformations with the DIC software, while the fifth marker in the top row is used to keep track of the x axis during the preparation prior mounting on the biaxial machine.

and allowed to thaw at room temperature (20°C). A schematic representation of the approximate sample location and corresponding nomenclature is shown in Fig. 1(a). This sample size is sufficient to allow for an accurate constitutive modeling of soft tissues through biaxial tests [42]. A side view image of the samples resting on a custom 3D printed template, as shown in Fig. 1(b), was acquired and used to measure the thickness in the open-source software Fiji [52]. The samples were then attached to four hooks (Ahrex, Denmark) on each side with a distance of ≈ 3 mm. On the epidermis side, four fiducial markers were placed in the center of the samples, enclosing an approximate area of 5 mm × 5 mm (Fig. 1(c)).

The samples were mounted on a custom-built biaxial machine [33] with surgical Gore-Tex CV5 sutures (Gore Medicals, USA) attached to the hooks. The machine was equipped with rotating bars on each arm, allowing the samples to balance during loading and minimizing shear stresses. The deformations were computed based on the position of the fiducial markers tracked with a custom digital image correlation (DIC) software [53], allowing us to obtain a complete description of planar deformations, including shear deformations due to material anisotropy. Data were synchronized with the measured forces at a frequency of 2 Hz. Throughout the tests, the samples were immersed in water bath filled with 0.1×phosphate buffered saline (PBS) solution at 37 °C.

After mounting, the samples were pre-loaded with 0.01 N in both the x and y directions, defining the zero-strain reference configuration, and preconditioned with 5 loading-unloading cycles with $d_x : d_y = 1 : 1$ at a rate of 0.1 mm/s, where d_x and d_y are the displacements along the x and y directions, respectively. Four loading protocols were then performed, each repeated three times at a rate of 0.1 mm/s: biaxial test 1 : 1, biaxial test with increased displacement along the less rigid direction $1 : \delta$, $0.75 \leq \delta \leq 1.25$, uniaxial test along x, and uniaxial test along y. In all tests, only the loading phase is recorded and used for the subsequent calibration of the mechanical models.

2.3. Second harmonic generation imaging and volume reconstruction

After completing the mechanical tests and within two hours from thawing, the samples were prepared for the second harmonic generation (SHG) imaging [55]. Samples were chemically fixated in 4% paraformaldehyde for at least 12 h to prevent tissue degradation and preserve collagen fiber structure. The samples were then optically cleared according to the SeeDBp protocol [56] to facilitate SHG imaging of deeper dermis layers. Clearing was carried out step by step by incubating the samples in 6 fructose solutions of increasing concentration at 25 °C. Specifically, the samples were incubated in a 20%, 40%, 60% w:v fructose:0.1×PBS solution for 4 h each and then in a 80% w:v fructose:0.1×PBS solution and 100% w:v fructose: distilled water solution for 12 h each. In the final step the samples were incubated in a fully saturated fructose solution (SeeDB solution), 80.2% w:w fructose:distilled water, for 24 h. This technique allows biological tissues to be cleared while preserving their morphology [57]. However, compared to other tissues documented in the literature [58], the treatment enhanced the clarity of the samples but complete transparency is not achieved. This is likely due to the increased density of the collagen network in the dermis layer. This makes it difficult for the solution to penetrate deep into the tissue. After the clearing process was completed, the samples were placed in a press-to-seal silicone isolator (CoverWell™ Imaging Chambers, Grace BIO-Labs, Oregon, USA) filled with SeeDB solution and sealed at the top and bottom with two rectangular glass coverslips ensuring no bubbles are placed over the acquisition site (Fig. 2(a)). To prevent any compression of the sample against the glasses, resulting in possible alterations of the fiber arrangement, silicone isolators were stacked to match the thickness of the sample. Sealing also prevents SeeDB to evaporate and increases its concentration, thereby altering the refractive index of the solution with negative impact on the quality of the image due to the increased light scattering.

SHG imaging was performed with a Leica TCS SP8 (Leica Microsystem, Germany) confocal multiphoton microscope using the Leica HCX IRAPO 25×, NA 0.95 water objective with a working distance of 2.4 mm. The second harmonic of collagen was induced with a multiphoton laser source tuned to 890 nm (Chameleon Ultra I; Coherent Corp., Saxonburg, PA, United States), while the signal emitted at 445 nm was detected in the forward and backward directions with standard photomultiplier tube (PMT) and highly sensitive HyD (GaAsP) detectors, respectively. No aperture was placed in front of the laser source, nor in front of the detectors. The scattering that occurred at greater depths in the tissue was compensated for by linearly increasing the laser power. Images were acquired on a 465 µm × 465 µm square target within the fiducial markers using an $x - y$ resolution of 0.454 μm/px (Fig. 2(b)). To enable a volume reconstruction of the target region, images are recorded every 0.57 µm in the z direction. This represents the lower system-optimized vertical step size in relation to image resolution, numerical aperture, refractive index, and acquisition wavelength. For the additional 4 samples from Patient 2, the 2-photon excited fluorescence (2PEF) signal was also recorded to observe the difference of elastin fiber content between the healthy and scarred samples. Due to the non-optimal transparency of the samples, only about 300 µm tissue thickness from the epidermis side could be scanned.

To compensate for the blurring in the lateral ($x - y$) and vertical (z) directions due to the inherent specimen-induced aberrations and light scattering, which could alter the results of the microstructural analysis, the SHG stacks were then deconvoluted. This

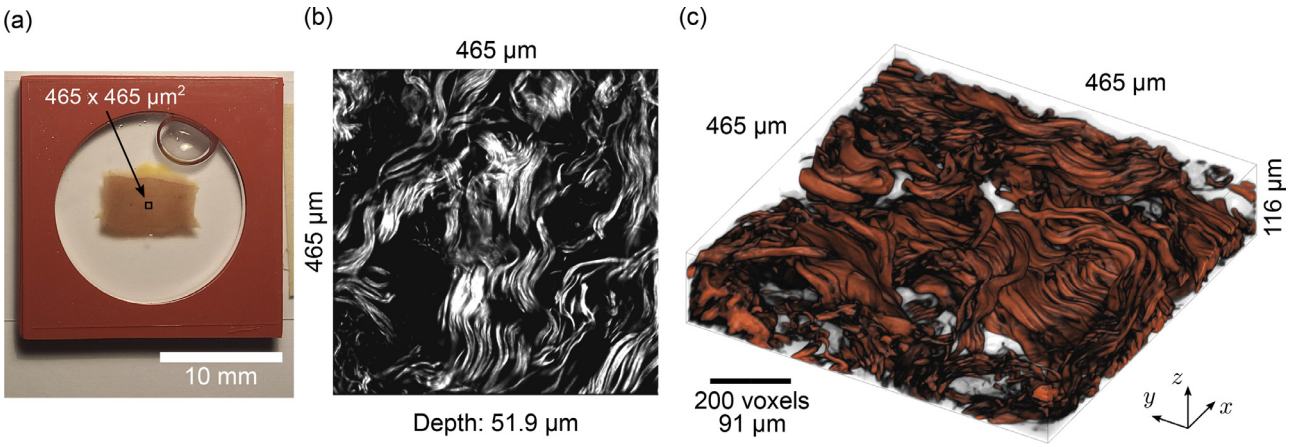

Fig. 2. SHG stack acquisition for volume reconstruction of collagen fibers: (a) sample ABL1-p3 (cropped) in the silicone isolator filled with See DB solution and the representative square SHG target (at scale); (b) representative 465 μm × 465 μm SHG image taken at 51.9 μm below the epidermis of the sample in (a); (c) representative collagen fiber volume of sample ABL1-p3 (first 116 μm for visualization purposes) after the deconvolution process with DeconvolutionLab2 [54].

procedure, applicable to SHG images [59], was performed in the open-source image processing software Fiji [52] using the DeconvolutionLab2 plugin for deconvolution microscopy [54]. In particular, the Richardson-Lucy algorithm with total variation regularization (regularization parameter $\lambda = 10^{-3}$, 25 iterations) was employed. The point spread function required for the process was derived using the Gibson and Lanny 3D optical model [60,61] adopting the refractive index of the collagen fibers in the SeeDB solution, $n_s = 1.48$ [62]. Finally, to achieve a uniform voxel size $\Delta x = \Delta y = \Delta z$ required for a consistent measurement of the fiber orientation distribution, the number of images along the z direction is increased so that the distance Δz is reduced from 0.57 μm to $\Delta x = \Delta y = 0.454$ μm. This reslicing process is performed in MATLAB with the built-in function `imresize3` by applying a stretch factor of $\Delta z/\Delta x = 1.255$ along the z direction and maintaining a stretch of 1 along the x and y directions and using a linear interpolation sampling scheme (Fig. 2(c)) [51].

2.4. Microstructural analysis of collagen fiber orientation

The microstructural data of the collagen fiber networks were measured from the SHG stacks using the algorithm described in our recent work [51]. The algorithm uses the directional information of the discrete 3D Fourier transform to obtain a detailed description of the fiber orientations over the three-dimensional angular domain. The result is a discrete fiber orientation distribution $d(\theta, \phi)$, where $\theta \in [-\pi/2, \pi/2]$ denotes the azimuthal angle from the x axis in the $x - y$ plane and $\phi \in [-\pi/2, \pi/2]$ its elevation angle. The distribution provides the normalized amount of fibers within a finite number of amplitude directions $\Delta\theta = \Delta\phi = 6^\circ$. Note that the angular domain is limited only to the right side of the spherical domain because fiber orientations can be described by both directions (θ, ϕ) and $(\theta + \pi, -\phi)$.

By introducing the Cartesian basis vectors $\{\mathbf{E}_1, \mathbf{E}_2, \mathbf{E}_3\}$, which are assumed to be coaxial with the x, y, z axes, respectively, a general fiber direction in the stress-free reference configuration can be described by the unit vector $\mathbf{N}(\theta, \phi) = \cos\phi\cos\theta\mathbf{E}_1 + \cos\phi\sin\theta\mathbf{E}_2 + \sin\phi\mathbf{E}_3$ (Fig. 3(a)). To obtain the relevant fiber distribution parameters required for the mechanical models (see Section 2.5), the distribution $d(\theta, \phi)$ was fitted with a combination of m distributions, each of the following representing a fiber family, according to

$$\rho(\mathbf{N}) = \sum_{i=1}^{m} \nu_i \rho_i(\mathbf{N}), \tag{1}$$

where ν_i represents the fiber family volume fraction ($\Sigma\nu_i = 1$), while $\rho_i(\mathbf{N}) = \rho_{\mathrm{ip},i}(\mathbf{N})\rho_{\mathrm{op},i}(\mathbf{N})$ is a bivariate distribution that depends on two independent in-plane and out-of-plane von Mises distributions, respectively defined as [30]

$$\rho_{\mathrm{ip},i}(\mathbf{N}) = \frac{\exp[a_i(2(\mathbf{N}\cdot\mathbf{M}_i/|\mathbf{N}_{\mathrm{ip}}|)^2 - 1)]}{I_0(a_i)},$$
$$\rho_{\mathrm{op},i}(\mathbf{N}) = 2\sqrt{\frac{2b_i}{\pi}}\frac{\exp[-2b_i(\mathbf{N}\cdot\mathbf{M}_{\mathrm{op},i})^2]}{\mathrm{erf}(\sqrt{2b_i})}. \tag{2}$$

Herein, the orthonormal basis vectors $\{\mathbf{M}_i, \mathbf{M}_{\mathrm{ip},i}, \mathbf{M}_{\mathrm{op},i}\}$ were introduced to identify the orientation of the ith fiber family in which the vector $\mathbf{M}_i$ represents the mean fiber direction, $\{\mathbf{M}_i, \mathbf{M}_{\mathrm{ip},i}\}$ defines the mean plane of the fiber family, and $\mathbf{M}_{\mathrm{op},i}$ is the out-of-plane normal. Accordingly, in Eq. $(2)_1$, $|\mathbf{N}_{\mathrm{ip}}|$ denotes the projection of $\mathbf{N}$ onto the $\{\mathbf{M}_i, \mathbf{M}_{\mathrm{ip},i}\}$ plane (Fig. 3(b)). The rotation of the principal basis of the fiber family relative to the Cartesian basis can be described with a triplet of angles α_i, β_i, γ_i, where the first two denote the azimuthal and elevation angle of the mean fiber direction, $\mathbf{M}_i = \mathbf{N}(\alpha_i, \beta_i)$, whereas the last one is the rotation of the frame about $\mathbf{M}_i$ (Fig. 3(c)). The constants a_i and b_i are parameters that define the in-plane and out-of-plane concentrations, respectively. The limit case of $a_i, b_i \to \infty$ corresponds to perfect fiber alignment along the mean fiber direction $\mathbf{M}_i$, while for $a_i, b_i \to 0$ an isotropic distribution is obtained. Finally, $I_0(\bullet)$ and $\mathrm{erf}(\bullet)$ are the zero-order Bessel function of type I, and the error function of $(\bullet)$, respectively, which ensure the normalization condition over the unit sphere $\mathbb{S}$, $\frac{1}{4\pi}\int_{\mathbb{S}} \rho_i(\mathbf{N})\mathrm{d}\mathbb{S} = 1$.

The particular choice for the distributions in Eq. (2) verifies the symmetry requirement for Eq. (1), i.e. $\rho(\mathbf{N}) = \rho(-\mathbf{N})$, or equivalently $\rho(\theta, \phi) = \rho(\theta + \pi, -\phi)$. Therefore, each fiber family is fully described by the parameter set $\{a_i, b_i, \alpha_i, \beta_i, \gamma_i, \nu_i\}$. Alternatively to a_i and b_i, the fiber dispersion can be described by two scalar dispersion parameters derived from Eq. (2), i.e.

$$\kappa_{\mathrm{ip},i} = \frac{1}{2}\left(1 - \frac{I_1(a_i)}{I_0(a_i)}\right), \quad \kappa_{\mathrm{op},i} = \frac{1}{2} - \frac{1}{8b_i} + \frac{1}{4}\sqrt{\frac{2}{\pi b_i}}\frac{\exp(-2b_i)}{\mathrm{erf}(\sqrt{2b_i})}, \tag{3}$$

where $0 \le \kappa_{\mathrm{ip},i} < 1/2$, and $1/3 \le \kappa_{\mathrm{op},i} \le 1/2$, for $a_i, b_i \ge 0$ [30].

To determine the number of families of each skin SHG stack, the measured distribution $d(\theta, \phi)$ was fitted stepwise with an increasing number of fiber families m until a quality of fit $R^2 > 0.9$ was achieved.

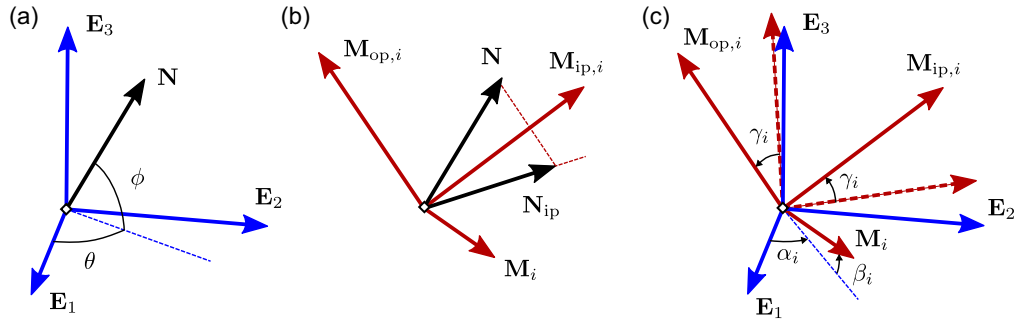

Fig. 3. Schematic representation of the orientation of the unit fiber $\mathbf{N}$ (in black), the global Cartesian basis $\{\mathbf{E}_1, \mathbf{E}_2, \mathbf{E}_3\}$ (in blue) and the principal fiber family basis $\{\mathbf{M}_i, \mathbf{M}_{\mathrm{ip},i}, \mathbf{M}_{\mathrm{op},i}\}$ (in red): (a) unit vector $\mathbf{N}$ in the global frame; (b) unit vector $\mathbf{N}$ in the principal fiber family basis and its projection $\mathbf{N}_{\mathrm{ip}}$ onto the mean fiber plane $\{\mathbf{M}_i, \mathbf{M}_{\mathrm{ip},i}\}$; (c) rotation of the principal basis with respect to the global basis using the angles α_i, β_i, γ_i. Dashed vectors represent $\mathbf{M}_{\mathrm{ip},i}$ and $\mathbf{M}_{\mathrm{op},i}$ before the rotation about $\mathbf{M}_i$.

2.5. Material model

We introduce the deformation gradient $\mathbf{F} = \partial\mathbf{x}/\partial\mathbf{X}$, which describes the deformation of a material point $\mathbf{X}$ from the stress-free reference configuration to a point $\mathbf{x}(\mathbf{X})$ in the deformed configuration. The right Cauchy-Green tensor is then calculated as $\mathbf{C} = \mathbf{F}^{\mathrm{T}}\mathbf{F}$. We describe the material as an incompressible superposition of an isotropic ground matrix, representing the ground substance and the elastin fibers, and an anisotropic dispersion of collagen fibers. Accordingly, we adopt a decoupled strain-energy function Ψ of the form

$$\Psi = \Psi_{\mathrm{g}} + \sum_{i=1}^{m} \nu_i \Psi_{\mathrm{f},i} - p(J-1), \qquad J = \det\mathbf{F} > 0, \tag{4}$$

where $\Psi_{\mathrm{g}}(\mathbf{C})$ is the isotropic ground matrix strain energy, $\Psi_{\mathrm{f},i}$ is the contribution of the i-th fiber family weighted by the volume fraction ν_i, and the last term is introduced to enforce the incompressibility constraint using a Lagrange multiplier p, representing a hydrostatic pressure.

Following [30], we use a neo-Hookean model for the ground matrix, i.e.

$$\Psi_{\mathrm{g}}(\mathbf{C}) = \frac{\mu}{2}(I_1 - 3), \qquad I_1 = \mathbf{C} : \mathbf{I}, \tag{5}$$

with μ representing the shear modulus at incipient deformation, I_1 the first invariant of $\mathbf{C}$, and $\mathbf{I}$ is the second-order identity tensor.

For the fiber strain energy, we adopt two different formulations, one using a generalized structure tensor (GST) approach and one using a discrete fiber dispersion (DFD) method. In the GST formulation, $\Psi_{\mathrm{f},i}$ is written as [30]

$$\Psi_{\mathrm{f},i} = \frac{k_1}{2k_2}\left\{\exp\left[k_2(I^*_{4,i} - 1)^2\right] - 1\right\}, \qquad I^*_{4,i} = \mathbf{C} : \mathbf{H}_i, \tag{6}$$

where k_1 is a stiffness-like parameter and k_2 a dimensionless parameter controlling the stiffening, while $I^*_{4,i}$ is a generalized fourth invariant weighted with the fiber family distribution. This quantity is computed using the structure tensor $\mathbf{H}_i$ depending on the in-plane and out-of-plane dispersion parameters (3), expressed as [30]

$$\begin{aligned}\mathbf{H}_i = {} & 2\kappa_{\mathrm{ip},i}\kappa_{\mathrm{op},i}\mathbf{I} + 2\kappa_{\mathrm{op},i}(1 - 2\kappa_{\mathrm{ip},i})\mathbf{M}_i \otimes \mathbf{M}_i \\ & + (1 - 2\kappa_{\mathrm{op},i} - 2\kappa_{\mathrm{ip},i}\kappa_{\mathrm{op},i})\mathbf{M}_{\mathrm{op},i} \otimes \mathbf{M}_{\mathrm{op},i}.\end{aligned} \tag{7}$$

In the DFD approach, the overall strain energy is given by the sum of the strain energy contributions of a finite number n of representative fiber directions over the unit sphere $\mathbb{S}$ [34], i.e.

$$\Psi_{\mathrm{f},i} = \sum_{j=1}^{n} \rho_{i,j}\Psi_j(I_{4,j}), \qquad I_{4,j} = \mathbf{C} : \mathbf{N}_j \otimes \mathbf{N}_j, \tag{8}$$

where $\rho_{i,j}$ is the relative amount of fibers within the subdomain $\Delta\mathbb{S}_j$ associated with the representative fiber direction $\mathbf{N}_j$, computed as

$$\rho_{i,j} = \frac{1}{4\pi}\int_{\Delta\mathbb{S}_j} \rho_i(\mathbf{N})\mathrm{d}\mathbb{S}, \qquad j = 1, \dots, n, \tag{9}$$

and Ψ_j is the single fiber strain energy, defined as

$$\Psi_j(I_{4,j}) = \begin{cases} \dfrac{c_1}{2c_2}\left\{\exp\left[c_2(I_{4,j} - 1)^2\right] - 1\right\}, & I_{4,j} \geq 1, \\ 0, & I_{4,j} < 1, \end{cases} \tag{10}$$

where c_1 and c_2 are two material parameters, analogous but not equivalent to k_1 and k_2. Eq. (10) is intended to exclude the negligible strain energy contribution of the compressed fibers when the fourth invariant $I_{4,j}$, which denotes the square of the stretch in the direction $\mathbf{N}_j$, is smaller than 1. Since $\rho_i(\mathbf{N})$ is normalized, it follows from Eq. (9) that $\sum_j \rho_{i,j} = 1$. Any discretization of the unit sphere $\mathbb{S}$ can be used to compute the weights $\rho_{i,j}$. Here we adopt the adaptive meshing algorithm proposed in [63], which iteratively refines the discretization using spherical triangles until each $\rho_{i,j}$ is smaller than a threshold $\rho_{\max} = 0.001$.

Note that the material parameters for both the GST and DFD formulations do not depend on the specific fiber family, as the material is assumed to consist of collagen fibers of the same type, whereas the families are introduced to approximate the measured fiber distribution $d(\theta, \phi)$.

The second Piola-Kirchhoff stress tensor $\mathbf{S}$ is determined by differentiating the strain-energy function with respect to $\mathbf{C}/2$ [64]. Therefore, from Eq. (4) we get

$$\mathbf{S} = 2\frac{\partial\Psi}{\partial\mathbf{C}} = \mathbf{S}_{\mathrm{g}} + \sum_{i=1}^{m} \nu_i\mathbf{S}_{\mathrm{f},i} - p\mathbf{C}^{-1}, \tag{11}$$

where $\mathbf{S}_{\mathrm{g}} = \mu\mathbf{I}$ is the contribution of the ground matrix and $\mathbf{S}_{\mathrm{f},i}$ is the stress component of the ith fiber family. By using the strain-energy functions in the Eqs. (6) and (8), the stress tensors for the GST and DFD models, respectively, read

$$\mathbf{S}_{\mathrm{f},i} = 2\frac{\partial\Psi_{\mathrm{f},i}}{\partial I^*_{4,i}}\mathbf{H}_i, \qquad \mathbf{S}_{\mathrm{f},i} = 2\sum_{j=1}^{n} \rho_{i,j}\frac{\partial\Psi_j}{\partial I_{4,j}}\mathbf{N}_j \otimes \mathbf{N}_j. \tag{12}$$

Then the first Piola-Kirchhoff stress tensor $\mathbf{P}$, which is used in the following to fit the models to the experimental mechanical data, is derived from the relationship $\mathbf{P} = \mathbf{FS}$ [64]. Therefore, from Eq. (11) we get

$$\mathbf{P} = \mu\mathbf{F} + \sum_{i=1}^{m} \nu_i\mathbf{F}\mathbf{S}_{\mathrm{f},i} - p\mathbf{F}^{-\mathrm{T}}. \tag{13}$$

Finally, the Cauchy stress tensor $\boldsymbol{\sigma}$ is obtained by right-handed multiplication of Eq. (13) with $J^{-1}\mathbf{F}^{\mathrm{T}}$.

The main advantage of the GST model is its computational efficiency, which lies in the ability of the structure tensor $\mathbf{H}_i$ to account for fiber dispersion regardless the deformation state. Therefore, $\mathbf{H}_i$ can be pre-computed and used throughout the analysis. On the other hand, the GST model includes all fibers and cannot exclude the compressed ones without compromising its efficiency. In this case, the DFD model is practical and provides a simple fiber exclusion criterion with a higher but reasonable computational cost [34].

We also emphasize that despite the similarities, the two models differ substantially and agree only in the case of perfectly aligned fibers, $a_i, b_i \to \infty$, or for $m \to \infty$. As a consequence, the two sets of mechanical parameters $\{k_1, k_2\}$ and $\{c_1, c_2\}$ are not interchangeable between the two models.

2.6. Model fitting

Planar tensile tests were performed before SHG imaging, thus without prior knowledge of the fiber distribution. Due to the configuration of the biaxial testing machine, the samples can deform freely during testing, allowing material anisotropy with shear deformations even when no shear stress is applied. Therefore, the experimental deformation gradient, say $\mathbf{F}^{\mathrm{e}}$, was computed from the position of the four markers placed on the sample surface and tracked using a DIC system. Assuming that the strain field between the markers is homogeneous, we computed the planar components of $\mathbf{F}^{\mathrm{e}}$ using a bi-linear iso-parametric element with 4 nodes, where the only non-planar component F_{zz} was determined from the incompressibility assumption $J = \det \mathbf{F}^{\mathrm{e}} = 1$ [44,65].

The nominal stress components of the experimental first Piola-Kirchhoff stress tensor $\mathbf{P}^{\mathrm{e}}$ were computed from the recorded forces f_x and f_y acquired during the loading phase. Given the relatively large length of the surgical sutures threads compared to the size of the samples, the applied forces produce negligible rotation (shear) during loading, so the tangential components are assumed to be zero. Therefore, the nominal Piola-Kirchhoff stress tensor is expressed as [44,65]

$$\left[\mathbf{P}^{\mathrm{e}}\right] = \mathrm{diag}\left[f_x/(t\, l_y),\ f_y/(t\, l_x),\ 0\right], \tag{14}$$

where t is the sample thickness, measured as described in Section 2.2, while l_x and l_y are the width and height of the sample relative to the area within the hooks (Fig. 1(c)), measured from the first DIC image of the test using Fiji [52].

Subsequently, the mechanical parameters of each sample were determined by simultaneously minimizing all 4 objective functions χ_{qr}, $q, r \in \{x, y\}$, defined as

$$\chi_{qr} = \sum_{k=1}^{K} (P^{\mathrm{e}}_{qr} - P_{qr}(\mathbf{F}^{\mathrm{e}}))^2_k, \tag{15}$$

including simultaneous mechanical data from the two biaxial tests ($d_x : d_y = 1 : 1, 1 : \delta$). In Eq. (15), K denotes the total number of data points between the two tests, while P_{qr} is the qr component of the theoretical first Piola-Kirchhoff stress tensor $\mathbf{P}$ in Eq. (13), in which the hydrostatic pressure p was expressed using the plane stress constraint $P_{zz} = 0$. From Eq. (14) it follows that this method also enforces the planar shear components to zero. Note that only the parameters μ, k_1, k_2 (for the GST model) and c_1, c_2 (for the DFD model) need to be fitted since the microstructural parameters are obtained from the SHG stack (Section 2.4).

The analysis was performed using a custom MATLAB code (v. R2023a; The MathWorks Inc., Natick, MA, USA) based on the built-in nonlinear least squares function `lsqnonlin` using the trust-region-reflective algorithm. To ensure convergence to the same set of fitted parameters, the analysis was repeated several times for each sample, initiating the process from different combinations of initial parameter values [33].

2.7. Statistical analysis

The metrics used to assess the goodness of fit are the coefficient of determination R^2 for the fiber orientation distributions data and the weighted mean absolute percentage error (wMAPE) for the mechanical data, defined as

$$\mathrm{wMAPE} = \sum_{q,r\in\{x,y\}} \frac{\sum_{k=1}^{K} w_k \dfrac{|P^{\mathrm{e}}_{qr} - P_{qr}|_k}{|P^{\mathrm{e}}_{qr}|_k}}{\sum_{k=1}^{K} w_k} = \sum_{q,r\in\{x,y\}} \frac{\sum_{k=1}^{K} |P^{\mathrm{e}}_{qr} - P_{qr}|_k}{\sum_{k=1}^{K} |P^{\mathrm{e}}_{qr}|_k} \tag{16}$$

in which the weights w_k were assumed to be equal to $|P^{\mathrm{e}}_{qr}|_k$. Differences between values associated with the GST and DFD models (mechanical parameters and wMAPE) were compared with paired t-tests, while significant linear correlations between the mechanical parameters were tested using the Pearson correlation coefficient. The analysis of the angular data was performed according to circular statistics and took into account the symmetry mentioned in Section 2.4, according to which (θ, ϕ) and $(\theta + 180^\circ, -\phi)$ represent the same orientation. Specifically, the Watson-Williams high concentration F-test was used to test the difference between the average collagen fiber orientation of the samples from the left and right sides of the human body. Differences and correlations were considered significant when the P-value was less than 0.05 (95% confidence). Data analyses were carried out employing the Real Statistics Resource Pack software [66].

3. Results

3.1. Healthy skin

Fig. 4 shows the measured distributions computed from the SHG stacks of 14 healthy skin samples and the corresponding fitted bivariate distributions $\rho(\theta, \phi)$. The mean fiber directions and standard deviations computed from the measured distributions are summarized in Table 1 together with the SHG-scanned skin thicknesses. After the clearing process with SeeDBp, 311.8 ± 50.7 µm tissue thickness could be scanned from the epidermis side. The SHG stacks only included the dermis layer because the epidermis does not contain collagen fibers. However, due to sub-optimal clearing, only the backward SHG signal was suitable to obtain collagen fiber volumes of satisfactory quality.

In particular, all samples showed a fiber distribution with low average elevations and small standard deviations, $\bar{\phi} = -2.6 \pm 2.2^\circ$ and $\sigma_\phi = 21.4 \pm 6.5^\circ$ for the right samples, and $\bar{\phi} = -0.8 \pm 1.7^\circ$ and $\sigma_\phi = 20.4 \pm 6.3^\circ$ for the left ones, with no significant differences between the two groups. This indicates that the fiber dispersions lie mainly in the $x - y$ plane, i.e. the skin mean plane. Looking to the azimuthal quantities, a symmetry is observed although not significant for either the mean angles or the standard deviation. In particular, the distributions for the right samples were mainly oriented downward, with average azimuth $\bar{\theta} = -82.8 \pm 27.4^\circ$, and mostly upwards for the left ones, $\bar{\theta} = 82.0 \pm 32.2^\circ$. Furthermore, as expected, the fiber distributions were broader in the azimuthal direction with a standard deviation of $\sigma_\theta = 38.9 \pm 13.8^\circ$ and $\sigma_\theta = 39.0 \pm 16.3^\circ$ for the right and left samples, respectively. Despite the limited number of samples, these observations revealed a fiber organization consistent with the Langer's lines in the lower abdominal region, see Fig. 5, which represent the cleavage lines, i.e. the average direction of the collagen fibers in the human body [14,67].

Table 2 summarizes the microstructural parameters of the fitted von Mises distributions $\rho(\theta, \phi)$ shown in Fig. 4 (wireframe plots). The families are sorted in descending order by volume fraction ν_i so that the first family has the largest contribution to the

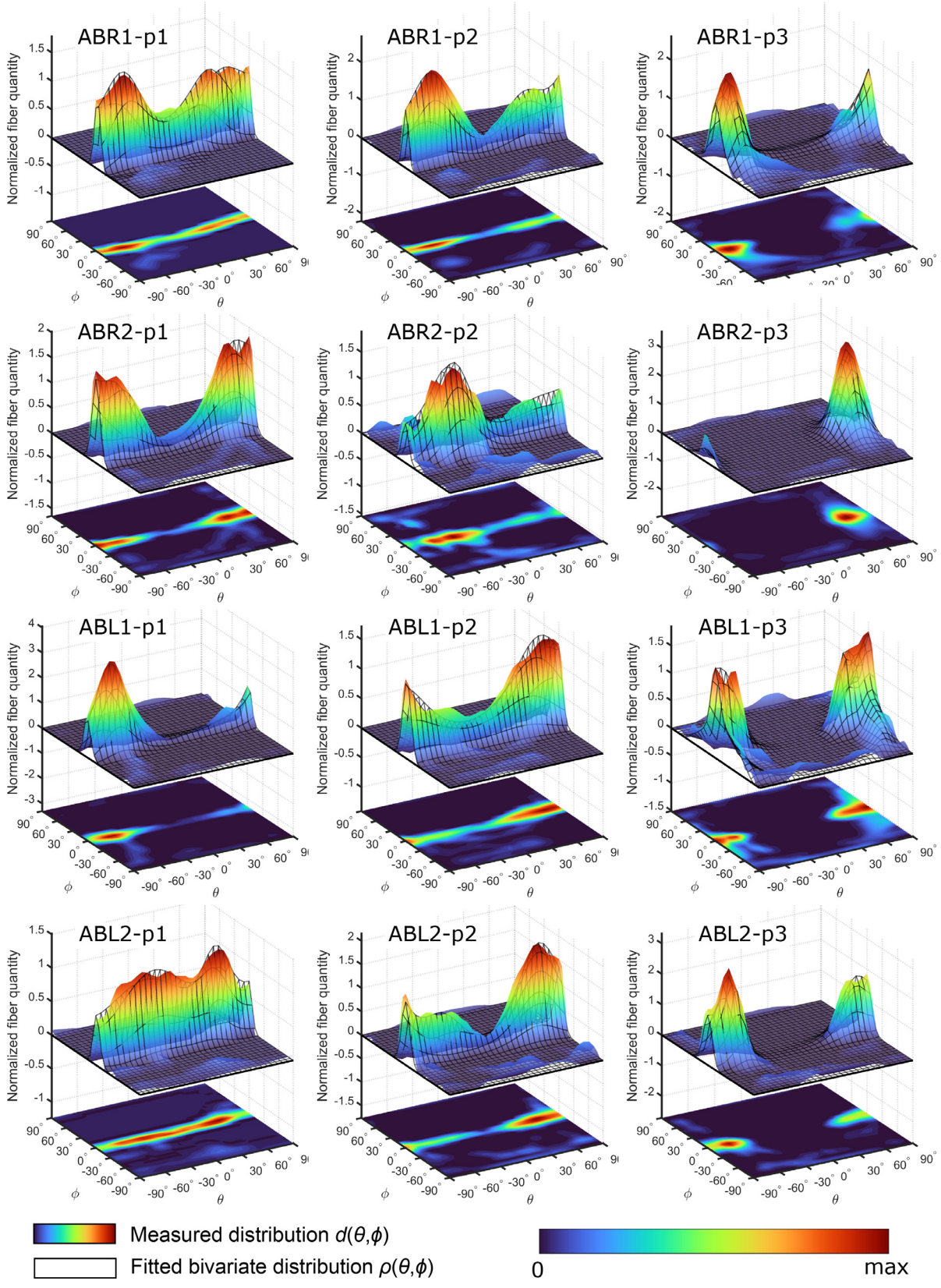

Fig. 4. Measured fiber orientation distributions $d(\theta,\phi)$ (colored), computed from the SHG stacks, and the fitted von Mises distributions $\rho(\theta,\phi)$ (wireframes) of the analyzed samples (results for ABR3-p1 and ABR4-p1 are here omitted). The distributions are normalized so that the integral over the unit hemisphere is one.

Table 1
Overall collagen fiber data determined from the SHG stacks: volume thickness t, average fiber azimuth $\bar{\theta}$ and elevation $\bar{\phi}$, circular standard deviations along the azimuth σ_θ and elevation σ_ϕ. Averages and standard deviations for the angular data are reported separately for the right (R) and left (L) samples.

Sample		t (μm)	$\bar{\theta}$ (°)	$\bar{\phi}$ (°)	σ_θ (°)	σ_ϕ (°)
ABR1-p1		301.7	−84.6	−3.8	56.1	11.8
ABR1-p2		271.9	−71.5	−1.6	54.9	14.4
ABR1-p3		381.3	−78.3	−4.9	47.2	19.4
ABR2-p1		350.6	82.4	−0.5	26.1	27.0
ABR2-p2		290.7	−41.8	−4.5	35.7	18.0
ABR2-p3		216.6	66.8	−2.5	41.3	28.8
ABR3-p1		360.8	−52.0	−4.6	16.2	23.8
ABR4-p1		322.1	57.6	1.9	33.8	27.9
ABL1-p1		238.8	−65.3	−0.6	42.7	16.6
ABL1-p2		258.8	68.9	0.2	26.4	18.9
ABL1-p3		312.9	80.8	2.0	45.0	14.7
ABL2-p1		344.9	9.4	−3.4	29.9	24.3
ABL2-p2		354.0	68.8	−2.1	23.1	31.4
ABL2-p3		360.2	−79.8	−0.7	67.1	16.5
Average	(R)	311.8	−82.8	−2.6	38.9	21.4
	(L)		82.0	−0.8	39.0	20.4
St. Dev.	(R)	50.7	27.4	2.2	13.8	6.5
	(L)		32.2	1.7	16.3	6.3

Table 2
Microstructural parameters of the fitted distributions in Fig. 4 and goodness of fit (R^2).

	Fiber family 1						Fiber family 2						Fiber family 3						
Sample	a_1 (-)	b_1 (-)	α_1 (°)	β_1 (°)	γ_1 (°)	ν_1 (-)	a_2 (-)	b_2 (-)	α_2 (°)	β_2 (°)	γ_2 (°)	ν_2 (-)	a_3 (-)	b_3 (-)	α_3 (°)	β_3 (°)	γ_3 (°)	ν_3 (-)	R^2
ABR1-p1	0.5	24.8	46.3	−3.8	8.5	0.63	1.9	17.9	−60.2	−6.2	−3.0	0.33	0.0	22.5	25.0	−16.4	44.4	0.04	0.98
ABR1-p2	0.3	19.0	71.9	−0.7	2.9	0.77	2.0	25.2	−52.3	−2.7	2.9	0.23							0.97
ABR1-p3	6.9	2.4	−74.4	−10.9	10.7	0.54	1.4	11.5	90.0	−0.5	1.3	0.46							0.89
ABR2-p1	1.4	10.9	69.5	−1.8	6.2	0.77	2.4	31.2	−61.4	−2.8	−4.5	0.23							0.95
ABR2-p2	2.1	8.5	−38.0	−6.0	−7.5	0.60	0.3	21.8	70.7	−1.1	1.1	0.40							0.84
ABR2-p3	6.0	3.6	66.8	−2.5	−4.7	1.00													0.93
ABR3-p1	1.4	8.5	−58.1	−4.1	12.6	0.45	11.0	0.2	−40.0	−26.9	12.4	0.33	0.0	21.3	90.0	2.0	−0.8	0.22	0.95
ABR4-p1	0.7	17.1	−84.7	−3.5	−5.1	0.54	2.1	10.3	45.4	2.0	22.6	0.46							0.96
ABL1-p1	3.1	13.7	−64.2	−1.2	−4.5	0.76	0.5	46.5	90.0	−3.4	1.7	0.24							0.95
ABL1-p2	0.6	11.8	68.7	0.2	7.0	1.00													0.95
ABL1-p3	1.7	7.9	90.0	4.6	5.0	0.77	3.9	13.8	55.7	−5.4	5.0	0.23							0.92
ABL2-p1	0.4	20.6	−26.6	−3.9	−1.1	0.79	2.9	13.5	52.5	1.8	17.6	0.21							0.97
ABL2-p2	1.4	11.4	64.9	−2.0	5.6	0.83	1.5	44.8	−45.9	−0.6	−4.3	0.17							0.93
ABL2-p3	2.3	12.9	77.8	−1.4	10.2	0.55	11.5	6.0	−65.3	−1.8	45.0	0.45							0.93

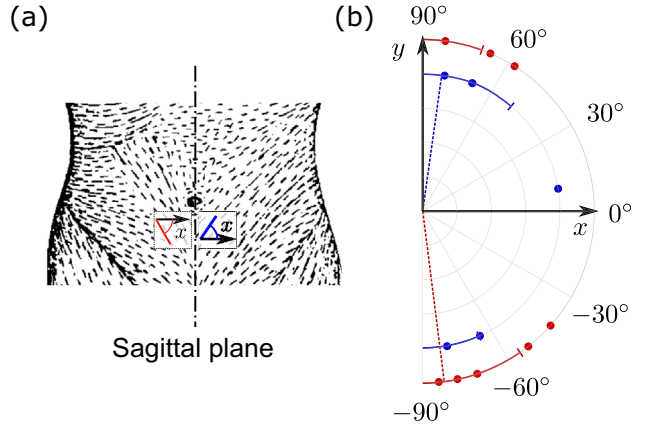

Fig. 5. Average collagen fiber orientation in the azimuthal direction: (a) Langer's lines [14], representing the average collagen fiber direction on the human body, and the highlighted directions in the abdominal region; (b) polar representation of the average fiber direction of the right (red dots) and left (blue dots) samples about the sagittal plane, computed from the measured fiber orientation distributions. Dashed lines represent the right and left averages directions at $\bar{\theta} = -82.8°$ and $\bar{\theta} = 82.0°$, respectively, while the whiskers their corresponding circular standard deviations. Averages and standard deviations are calculated considering the orientation symmetry of the fibers, where $\theta = 90°$ and $\theta = -90°$ represent the same direction.

overall fiber orientation distribution. Recall that the fitting made no assumptions about the number m of families, which was obtained by the lower integer m that ensured a coefficient of determination $R^2 > 0.9$. In general, the number of families is reflected in the number of distinct local maxima, which in our cases was always $m \leq 2$. However, a third isotropic family was introduced for samples ABR1-p1 and ABR3-p1 (the latter is not shown in Fig. 4). This family, which represents the smallest volume fraction of the overall distribution with $\nu_3 = 0.04$ for ABR1-p1, and $\nu_3 = 0.22$ for ABR3-p1, does not relate to a local maximum, but rather shifts the distribution to improve the quality of the fit.

The mechanical parameters of the GST and DFD models are reported in Table 3 along with the sample thickness and the residual errors of the fitting expressed as wMAPE. Representative experimental mechanical responses in terms of principal Cauchy stresses and principal stretches are shown in Fig. 6 along with the predictions of the mechanical models. The sample thickness, measured from the side view images taken before the mechanical tests, was $t = 2.92 \pm 0.71$ mm. The shear parameter of the neo-Hookean ground matrix, which prevails at small stretches, was relatively small, $\mu = 1.142 \pm 0.879$ kPa. The fiber parameters were instead $k_1 = 0.5914 \pm 1.3013$ kPa and $k_2 = 68.5 \pm 29.5$ for the GST model and $c_1 = 1.9074 \pm 2.4427$ kPa and $c_2 = 43.6 \pm 15.3$ for the DFD model. As reported in Fig. 7(a), the fiber stiffness-like parameters k_1 were significantly lower than c_1 upon *log*-transformation

Table 3
Estimated mechanical parameters of the GST and DFD models from the biaxial tests and the relative mechanical fitting residual wMAPE error. The sample thickness is given in the first column.

			GST model			DFD model		
Sample	t (mm)	μ (kPa)	k_1 (kPa)	k_2 (-)	wMAPE (%)	c_1 (kPa)	c_2 (-)	wMAPE (%)
ABR1-p1	3.80	0.680	0.8736	53.7	30.0	3.3788	32.8	45.9
ABR1-p2	2.67	1.251	0.1267	52.1	28.7	1.2388	36.5	36.5
ABR1-p3	3.97	0.503	0.0300	48.5	31.5	0.7713	23.1	34.8
ABR2-p1	2.74	0.628	4.8057	66.9	50.9	8.2124	71.0	33.8
ABR2-p2	3.00	0.848	0.0497	34.4	37.1	0.5141	26.0	33.4
ABR2-p3	4.22	0.115	0.1292	63.3	24.0	4.6846	35.0	26.9
ABR3-p1	2.34	1.143	0.0166	130.0	28.0	0.5893	49.5	41.2
ABR4-p1	2.43	2.486	0.0233	102.5	20.2	0.6629	53.8	44.9
ABL1-p1	2.03	1.531	0.0205	91.5	42.8	0.0891	45.5	37.9
ABL1-p2	2.92	0.344	0.0003	51.0	37.8	0.3085	32.5	47.8
ABL1-p3	3.58	1.643	0.5251	74.9	29.0	1.3303	56.8	37.6
ABL2-p1	2.09	0.802	0.0020	38.3	38.7	0.0060	29.7	42.5
ABL2-p2	2.25	0.667	0.0215	41.0	26.3	0.1620	48.6	43.3
ABL2-p3	2.77	3.340	1.6553	110.8	34.4	4.7554	69.3	35.5
Average	2.92	1.142	0.5914	68.5	32.8	1.9074	43.6	38.7
St. Dev.	0.71	0.879	1.3013	29.5	8.1	2.4427	15.3	5.8

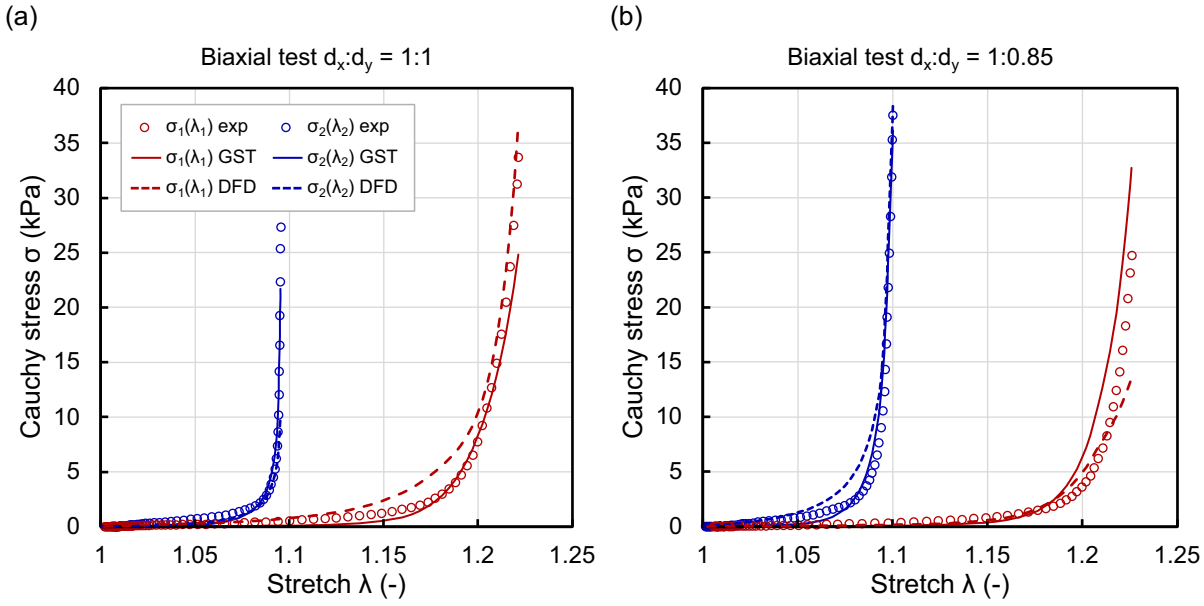

Fig. 6. Representative experimental mechanical response of sample ABR2-p3 (circles) in horizontal (red) and vertical directions (blue) for the biaxial tests (a) $d_x : d_y = 1 : 1$, and (b) $d_x : d_y = 1 : 0.85$ (loading curves). The mechanical models predicted the experimental data well, with a residual wMAPE error of 24% for the GST model (solid curves) and 26.85% for the DFD model (dashed curves). Note that each model used a unique set of parameters to predict both biaxial tests.

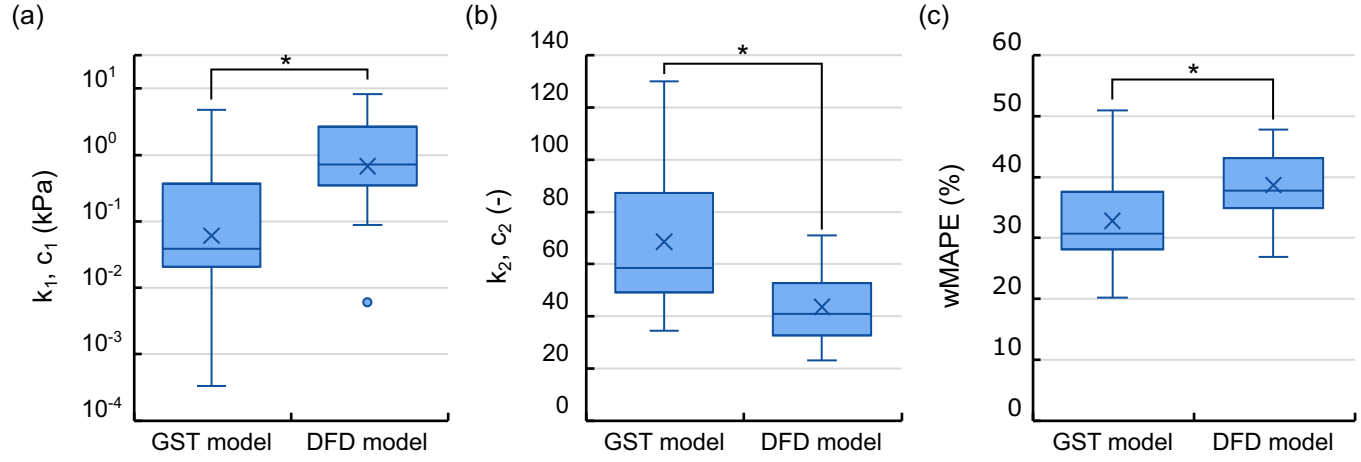

Fig. 7. Box-and-whiskers plots of GST and DFD parameters: (a) fiber stiffness-like parameters k_1, c_1; (b) stiffening parameters k_2, c_2; (c) mechanical fitting of the resudal wMAPE errors. The boxes extend from the lower to the upper quartile of the data, with a line at the median and whiskers extending to the minimum and maximum values. Crosses indicate the average values, circles the outliers ($*$: $P < 0.05$).

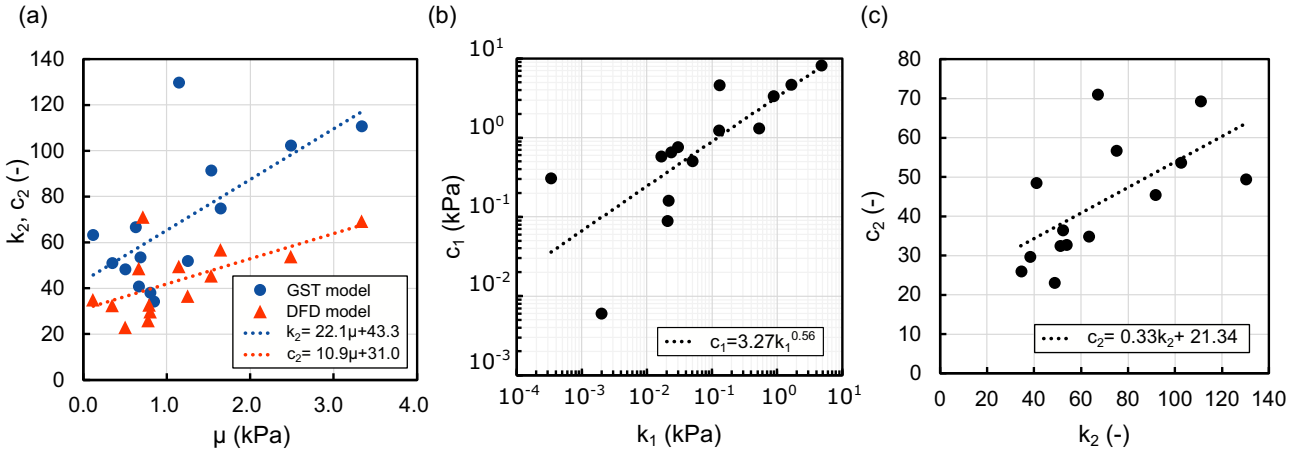

Fig. 8. Significant correlation between the parameters: (a) isotropic neo-Hookean parameter μ for the ground matrix with stiffening parameters k_2 and c_2; (b) fiber stiffness-like parameter k_1 with c_1; (c) stiffening parameter k_2 with c_2. In (b) the exponential relationship between k_1 and c_1 is obtained from linear regression in the *log*-transformed domain.

($P = 5.45 \times 10^{-5}$). On the other hand, the dimensionless parameter k_2, which controls the exponential stiffening of the loading curves, was significantly higher than its counterpart c_2 ($P = 7.39 \times 10^{-4}$) (Fig. 7(b)). This suggests a stiffer behavior of the DFD model compared to the GST one. However, as shown in Fig. 6, both constitutive models predicted the mechanical behavior of the skin with good agreement, although the DFD model proved more difficult to fit and displayed a residual wMAPE error of $38.7 \pm 5.8\%$, significantly higher ($P = 0.028$) than the error of the GST model, $32.8 \pm 8.1\%$ (Fig. 7(c)).

To examine possible correlations between mechanical and microstructural parameters, a linear regression analysis was carried out. Significant correlations were found between μ and k_2, c_2, shown in Fig. 8(a), with a Pearson coefficient of $r = 0.657$ ($P = 0.011$) and $r = 0.624$ ($P = 0.017$), respectively. Two additional correlations were found between the GST and DFD parameters. In particular, k_1 was positively correlated with c_1 in the *log*-transformation ($r = 0.773$, $P = 0.0012$) (Fig. 8(b)), as well as k_2 with c_2 ($r = 0.627$, $P = 0.016$) (Fig. 8(c)). Other nonlinear correlation between mechanical parameters were tested but no significant correlations were found.

In addition to the biaxial tests, we also performed uniaxial tests along the x and y directions to understand the mechanical behavior of the skin in the uniaxial tension regime. The mechanical responses along the x and y directions of all samples are shown in Fig. 9(a) and (b), respectively, while in Fig. 9(c) and (d), the respective principal stretches are shown. Therein, λ_1 and λ_2 were computed from the eigenvalues of the planar components of $\mathbf{F}^e$, i.e. using the position of the fiducial markers, whereas the out-of-plane stretch λ_3 was derived from the incompressibility assumption $J = \lambda_1\lambda_2\lambda_3 = 1$. Note that in Fig. 9(c) and (d) the data are truncated at axial stretches $\lambda_1 = 1.29$ and $\lambda_1 = 1.38$ to ensure a computation of the averages and standard deviations using at least 20 tests. The transverse stretches λ_2 and λ_1, relative to the tests along the x and y directions, both decrease as the samples elongate along the loading axis, except for a small region within the standard deviation above $\lambda = 1$. This unexpected behavior, more pronounced in the tests along the x direction (Fig. 9(c)), was probably caused by the movement of the samples from the bottom of the bath towards the DIC camera before reaching the stable height. During this vertical excursion (about 20 mm), the samples changed focal plane and the fiducial markers were magnified and appeared to be biaxially stretched. However, as soon as the samples reached the steady height relative to the camera, the actual movement of the markers was captured and the transverse stretches returned to a state of contraction ($\lambda < 1$). On the other hand, in both tests, the out-of-plane stretch λ_3 initially decreased to about 0.9 for axial stretches of $\lambda_1 = 1.16$ and $\lambda_2 = 1.23$. Subsequently, the trend was reversed and it expanded with increasing axial deformation. This behavior, however, seems unlikely in reality and is probably the result of the incompressibility assumption.

3.2. Scarred skin

Four additional samples were analyzed from Patient 2, who reported an older C-Section scar. Two samples from the right and left sides around the sagittal plane, SR-p2 and SL-p2, were tested with the scar running along the x direction. Two additional samples of adjacent healthy skin, HR-p2 and HL-p2, taken with the same orientation parallel to the scar were tested for comparison (Fig. 1(a)).

The SHG images revealed a consistent difference in collagen morphology between healthy and scarred tissues. As shown in Fig. 10(a) and (b), the collagen fiber bundles (in green) in scarred skin were straighter and thinner, running almost perpendicular to the scar axis and with increased concentration. This difference is also captured by the measured fiber orientation distributions shown in Fig. 10(c) and (d). In contrast to the healthy sample HR-p2, which has two nearly symmetrical fiber families with mean orientations $\alpha_1 = -83.9^\circ$ and $\alpha_2 = 46.9^\circ$, the scarred tissue presents a main family with high concentration at $\alpha_1 = -72.2^\circ$, along with a smaller but highly concentrated family almost parallel to the scar at $\alpha_2 = -8.1^\circ$. Similar results were observed for the other two samples (see Table 4). Although the focus of our study was primarily on collagen fibers, we observed a remarkable reduction in elastin fibers in the scarred skin (red fibers in Fig. 10(a) and (b)).

The mechanical parameters obtained from biaxial tests are listed in the Table 5. Due to the limited number of samples and the different location on the body, these parameters are not compared to the parameters presented in the previous section.

4. Discussion

In this study, 14 human skin samples from the lower abdominal region and 4 samples, 2 healthy and 2 scarred, from an older Cesarean section scar, were analyzed (Fig. 1). The microstructural parameters describing the organization of collagen fibers were obtained from SHG stacks taken at a square window of 465 μm ×

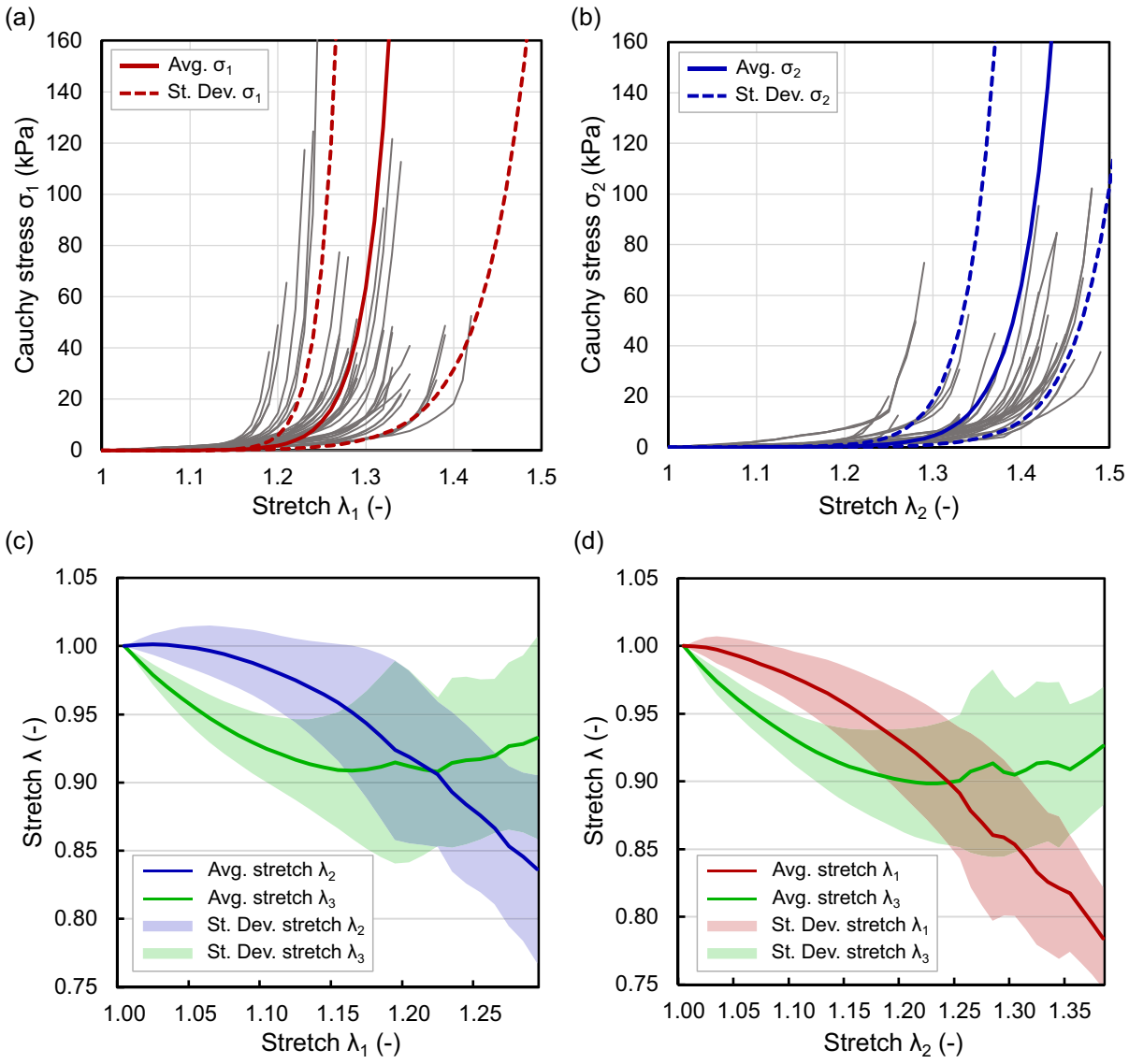

Fig. 9. Average mechanical responses of the uniaxial tests performed along the horizontal (x-axis) and vertical (y-axis) directions (loading curves): (a), (b) principal Cauchy stress σ versus principal stretch λ along x and y, respectively. Solid curves indicate the average values and dashed curves the standard deviations; (c), (d) transversal stretches λ_2, λ_1, and out-of-plane stretch λ_3 versus axial principal stretches along x and y. Averages and standard deviations computed from at least 20 tests.

Table 4
Microstructural parameters of the scarred skin samples and relative control samples of healthy skin. The last column indicates the goodness of fit (R^2).

	Fiber family 1						Fiber family 2						
Sample	a_1 (-)	b_1 (-)	α_1 (°)	β_1 (°)	γ_1 (°)	ν_1 (-)	a_2 (-)	b_2 (-)	α_2 (°)	β_2 (°)	γ_2 (°)	ν_2 (-)	R^2
SR-p2	4.1	18.7	−72.2	1.0	−7.1	0.77	15.4	38.2	−8.1	−3.0	−43.6	0.23	0.90
SL-p2	6.8	16.0	58.0	13.5	−16.4	0.74	5.0	12.9	−88.5	−1.3	−1.9	0.26	0.91
HR-p2	1.5	14.2	−83.9	0.2	−2.6	0.64	3.8	9.1	46.9	3.3	24.3	0.36	0.91
HL-p2	1.1	18.0	−76.7	−0.7	−2.5	0.57	3.7	8.5	46.4	−2.0	−0.1	0.43	0.94

Table 5
Estimated mechanical parameters and fitting residual wMAPE error of the scarred skin samples and the healthy control skin samples. The sample thickness is given in the first column.

			GST model			DFD model		
Sample	t (mm)	μ (kPa)	k_1 (kPa)	k_2 (-)	wMAPE (%)	c_1 (kPa)	c_2 (-)	wMAPE (%)
SR-p2	2.04	1.311	0.0106	28.9	68.5	0.0148	23.2	41.9
SL-p2	2.46	0.645	0.0079	37.4	37.3	0.1185	26.1	30.8
HR-p2	1.12	3.273	0.0197	129.3	33.4	3.8832	30.6	47.6
HL-p2	2.25	0.696	0.0930	22.8	20.1	0.7592	13.8	33.9

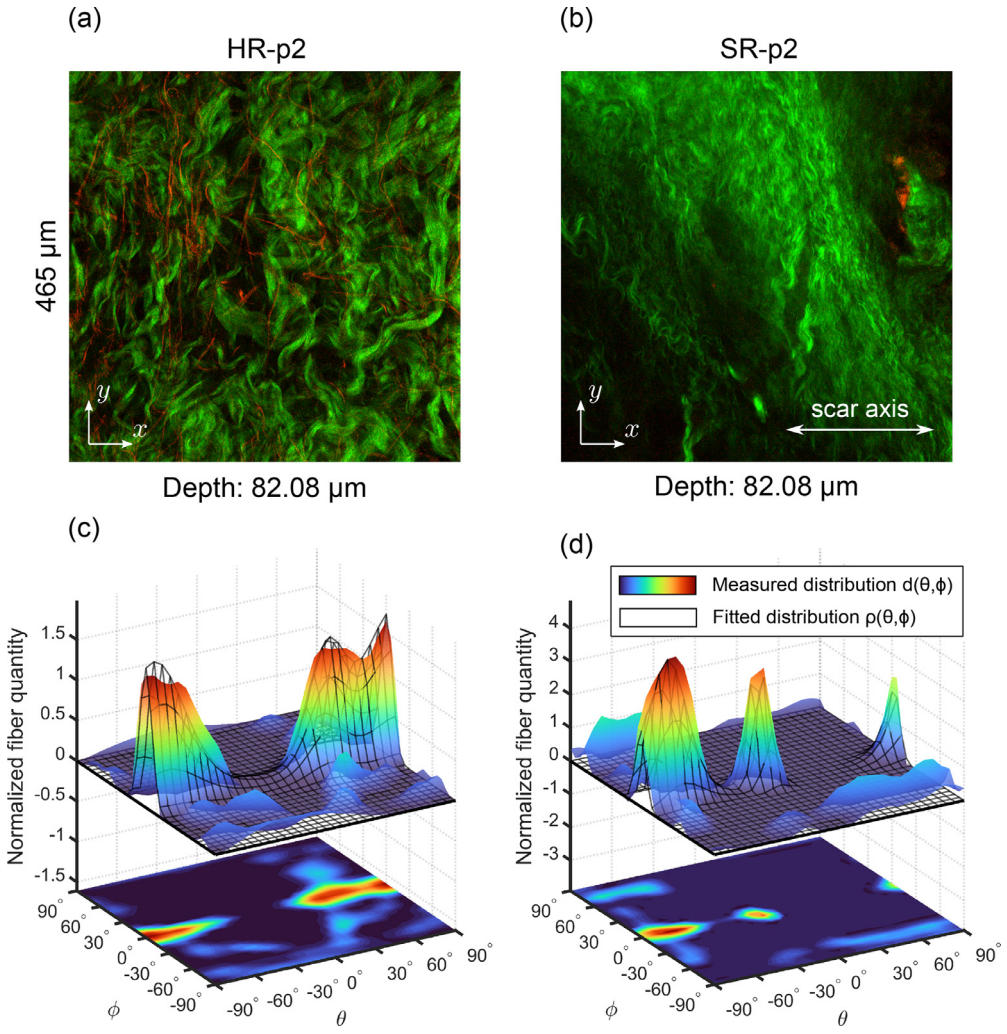

Fig. 10. Fiber architecture in healthy and scarred skin: (a),(b) superposition of collagen (SHG signal, green) and elastin fibers (2PEF signal, red) of the healthy (left) and scarred skin samples (right) HR-p2 and SR-p2, at 82.08 µm below the epidermis; (c),(d) orientation distribution of collagen fibers $d(\theta,\phi)$ (colored) and fitted von Mises distributions $\rho(\theta,\phi)$ (wireframes) of samples HR-p2 and SR-p2.

465 µm. By clearing the tissue with SeeDBp, we were able to scan skin collagen to an average depth of 311.8 µm, whereas under normal conditions only the first 100 µm are visible [57,68]. Despite the improvement, this only represented about 10% of the total skin thickness ($t = 2.92 \pm 0.71$ mm). This technique has the advantage of preserving collagen morphology as well as SHG and 2PEF signals using a simple protocol based on a non-toxic fructose solution. On the other hand, it seems to have little effect on dense collagenous tissue. SeeDB (See Deep Brain), originally developed to clear the entire brain of the mouse [56], was successfully applied to diseased human mitral valve leaflets, allowing scanning up to 1400 µm thickness [58], but achieved similar results when applied to tendons and cartilage ($\sim$ 300 µm visible thickness) [69]. To the best of our knowledge, this is the first time SeeDB was applied to skin tissue [70]. Other techniques such as benzylalcohol/benzylbenzoate (BABB) solutions were found to be more effective in clearing human skin [71], but caused shrinkage effects that could potentially affect the distribution of collagen fibers [72].

Collagen SHG stacks were analyzed after a post-processing deconvolution step using an algorithm based on the discrete 3D Fourier transform [51], which provided a complete description of the fiber orientation distribution $d(\theta,\phi)$ over the unit hemisphere for each sample. Even if the SHG stacks are not captured with polarization-resolved SHG (pSHG), which provides a comprehensive imaging of the collagen fibers along the entire planar direction, the algorithm still detects all visible fibers in the stacks, regardless of the intensity variability of the fiber signal due to the polarization angle of the laser. The analysis revealed that collagen architecture in most samples is characterized by a mixture of two non-symmetrical fiber families with different volume fractions although only one family was observed in samples ABR2-p3 and ABL1-p2. As in other membrane tissues, e.g., in the aortic walls [31], collagen fibers displayed an almost planar dispersion, highly concentrated in the midplane of the membrane. From a mechanical perspective, this provides the skin the tensile strength it needs to fulfill its membrane function. Considering the azimuthal orientation, the right and left samples showed symmetrical average orientations at $\bar{\theta} = -82.8 \pm 27.4^{\circ}$ and $\bar{\theta} = 82.0 \pm 32.2^{\circ}$, respectively, although the difference was not significant. This finding is consistent with the orientation of the Langer's lines in the lower abdominal region. These were first analyzed in 1861 by the Austrian doctor Karl Langer [14] and are the result of puncturing several points on the surface of skin cadavers with a round tool, observing the direction of their ovalization. The common interpretation of this phenomenon is attributed to collagen fibers separating along their mean direction when it is penetrated by a rigid body [73]. Our results, in accordance with similar studies on skin samples [74], confirms this thesis, although Langer's lines are sometimes attributed

to natural skin tension on the human body [75], and not related to the collagen direction [76].

Specific microstructural parameters for each family were quantified by fitting a combination $\rho(\theta,\phi)$ of bivariate von Mises distributions to the measured distribution $d(\theta,\phi)$. These parameters were used to fit two mechanical models to the mechanical data from the biaxial tests by assuming that the distributions measured from the SHG stacks were representative of the whole sample volume. The model introduced by Holzapfel et al. [30] for modeling arterial walls employs a generalized structure tensor (GST) approach, while the model introduced by Li et al. [34] is based on a discrete fiber dispersion (DFD) method. The shear modulus μ of the neo-Hookean ground matrix, which is the same for both models, was $\mu = 1.142 \pm 0.879$ kPa. The parameters of the GST model were $k_1 = 0.5914 \pm 1.3013$ kPa and $k_2 = 68.5 \pm 29.5$. These results are of the same order of magnitude as those reported by Tonge et al. [47] for human dorsal skin. The authors obtained $k_1 = 1.446 \pm 2.040$ kPa and $k_2 = 76.1 \pm 71.0$ from full-field bulge tests assuming planar fiber dispersion. Similar parameters were also obtained by Wei et al. [39] from *in vivo* indentation tests on facial skin, $k_1 = 2.402$ kPa and $k_2 = 15.9$. Regarding the DFD model, the fitted parameters are $c_1 = 1.9074 \pm 2.4427$ kPa and $c_2 = 43.6 \pm 15.3$. Overall, both models predicted the mechanical behavior of the skin well, although the GST model was found to be more accurate and had significantly lower residual error. This might indicate that the GST model is more adequate to model the mechanical response of the skin, but more investigations are needed to understand whether this holds true for skin samples from other body locations, also in relation to age, sex, and health condition of the patients.

As mentioned in Section 2.5, the GST and DFD models differ substantially, although the two strain-energy definitions in Eq. (6) and (10) have a similar form. Therefore, the parameter sets cannot be interchanged between the models, except in the special case of perfectly aligned fiber families [77]. This difference was demonstrated by the significant differences between $k_1 - c_1$ ($P = 5.45 \times 10^{-5}$) and $k_2 - c_2$ ($P = 7.39 \times 10^{-4}$). Nevertheless, the significant correlations between $k_1 - c_1$ ($r = 0.773$, $P = 0.0012$) and $k_2 - c_2$ ($r = 0.627$, $P = 0.016$), reported in Fig. 8(b) and (c), could be helpful in transferring the parameters from one model to the other. Further significant correlations emerged between μ and the parameters k_2 and c_2, which could suggest a mechanical connection between the ground matrix and the embedded collagen fibers.

It is important to mention that the mechanical tests were performed assuming that the reference configuration is the pre-loaded one with 0.01 N, i.e. the smallest measurable force of our load cell, both horizontally and vertically. Therefore, the obtained parameters must be related to the pre-loaded *ex vivo* configuration. Recent studies on murine skin analyzed the influence of different reference configurations on the final mechanical parameters and showed a significant variation between the parameters associated with the *ex vivo* pre-loaded and the *in vivo* unloaded configurations [49]. Since it was not possible to measure the residual strains during the physiological pre-loading of the skin in the living state, only the *ex vivo* configuration was considered as a reference.

In this study, the skin was assumed to be incompressible. This approximation, first introduced by Lanir and Fung [7], is commonly used in mechanical modeling of several soft tissues, including aortic walls [31], mitral valve leaflets [33] and brain tissue [78]. This makes the fitting process of the mechanical models easier by allowing the explicit expression of λ_3 from the planar and measurable stretch components λ_1 and λ_2, which otherwise would require a dedicated measurement. However, recent studies on skin under uniaxial deformation, measuring λ_3 from side view images of the sample, showed a significant volume loss of up to 30% at uniaxial stretches $\lambda = 1.2$, which is related to dehydration depending on the osmolarity of the environment [79,80]. To better understand the effect of the incompressibility assumption in our analysis, uniaxial tests were performed along the x and y directions. Consistent with the observation of Wahlsten et al. [80], our tests showed a strong transversal contraction, with an average in-plane transverse stretch of $\lambda \approx 0.85$ at a uniaxial stretch of $\lambda = 1.3$ (see Fig. 9(c),(d)). In response, the out-of-plane stretch λ_3, computed from the incompressibility constraint $J = \lambda_1\lambda_2\lambda_3 = 1$, transitioned from a contraction phase at low uniaxial stretches to an expansion trend beyond $\lambda = 1.16 \div 1.23$. Notably, this was observed in both the x and y directions. Since this behavior is unlikely, our results might suggest that the volumetric changes no longer become negligible at high deformation levels. It is important to mention that our uniaxial tests are performed using square specimens and not standardized shapes, like, e.g., T-bone or dog-bone specimens. However, in uniaxial tests, we found that the rotating bars on the biaxial machine arms (see Section 2.2) ensure an even distribution of the forces between the hooks, thus allowing a uniaxial distribution of stresses in the specimen within the fiducial markers. Subsequently, the displacements of the fiducial markers are measured using the DIC, which allowed us to compute the stretch component in the direction of the applied uniaxial load, even though shear deformation could occur due to the anisotropic behavior of the specimens.

Finally, two scarred and two healthy samples from an old Cesarean section from Patient 2 were analyzed. The measured fiber distributions $d(\theta,\phi)$ revealed that the collagen fibers in the scarred tissue are more concentrated and are mainly located transversely to the scar axis. This finding is consistent with other SHG analyses on pathological skin tissue [81,82]. In addition, a strong loss of elastin fibers was observed in the 2PEF signal (Fig. 10(a),(b)). Early studies on elastin in skin demonstrated that it plays a role at low strains and is responsible for the recoiling mechanism of the collagen fibers after deformation [9]. During the wound healing process the regeneration of elastin fibers follows that of collagen fibers. The compact organization of collagen prevents the complete formation of an elastic fiber network in the scarred tissue, causing the overall elasticity to decrease [83]. In our analysis this stiffness difference cannot be determined due to the limited number of scar samples tested. Nonetheless, considering the relevant implications of a reduced elastin fibers content on the overall mechanical behavior as reported by Zhou et al. [19], our observations point out the importance of including elastin in the mechanical modeling.

5. Conclusions

Skin is a complex tissue that plays an essential role in maintaining the integrity of the human body. It is of fundamental importance to investigate the mechanical properties of skin for the model development and predictive simulations. To obtain the fundamental mechanical and microstructural parameters for the GST and DFD models, a campaign of experimental tests on 14 *ex vivo* human skin samples were conducted from the abdominal region. Microstructural parameters were computed from SHG stacks of collagen fibers, while mechanical parameters were determined by fitting the models to the measured stress-strain responses from biaxial tests. Further uniaxial tests were performed to investigate the volumetric behavior of the skin. The out-of-plane stretch obtained from the in-plane stretches using the incompressibility constraint led to an unexpected expansion at high levels of uniaxial deformation, thereby questioning the incompressibility hypothesis often advocated in the mechanical modeling of skin. Although our results are not supported by out-of-plane measurements, they appear to confirm the results of Wahlsten et al. [80]. Finally, qualitative analysis on scarred skin samples revealed a significant re-

duction in elastin fiber content. Considering the lower stiffness of scarred tissue [3], this observation points to the role of elastin fibers in providing elasticity to the skin.

Declaration of competing interest

The authors declare that they have no known competing financial interests or personal relationships that could have appeared to influence the work reported in this paper.

CRediT authorship contribution statement

Riccardo Alberini: Writing – original draft, Visualization, Software, Investigation. **Andrea Spagnoli:** Supervision, Writing – review & editing. **Mohammad Javad Sadeghinia:** Writing – review & editing, Investigation. **Bjorn Skallerud:** Writing – review & editing, Resources. **Michele Terzano:** Writing – review & editing, Investigation. **Gerhard A. Holzapfel:** Writing – review & editing, Supervision.

References

[1] J.E. Lai-Cheong, J.A. McGrath, Structure and function of skin, hair and nails, Medicine 41 (6) (2013) 317–320, doi:10.1016/j.mpmed.2013.04.017.

[2] F. Martini, J. Nath, Anatomy & Physiology, Benjamin Cummings, San Francisco, 2010. https://books.google.it/books?id=dlz9ZwEACAAJ

[3] T. Burns, A. Rook, Rook's textbook of dermatology, Blackwell Publishing, Hoboken, 2008.

[4] G.D. Weinstein, R.J. Boucek, Collagen and elastin of human dermis, J. Invest. Dermatol. 35 (4) (1960) 227–229, doi:10.1038/jid.1960.109.

[5] J.W. Jor, M.D. Parker, A.J. Taberner, M.P. Nash, P.M. Nielsen, Computational and experimental characterization of skin mechanics: identifying current challenges and future directions, Wiley Interdiscip. Rev. Syst. Biol. Med. 5 (5) (2013) 539–556, doi:10.1002/wsbm.1228.

[6] J.M. Benítez, F.J. Montáns, The mechanical behavior of skin: structures and models for the finite element analysis, Comput. Struct. 190 (2017) 75–107, doi:10.1016/j.compstruc.2017.05.003.

[7] Y. Lanir, Y. Fung, Two-dimensional mechanical properties of rabbit skin—II. Experimental results, J. Biomech. 7 (2) (1974) 171–182, doi:10.1016/0021-9290(74)90058-X.

[8] C.H. Daly, Biomechanical properties of dermis, J. Invest. Dermatol. 79 (1) (1982) 17–20, doi:10.1038/jid.1982.4.

[9] H. Oxlund, J. Manschot, A. Viidik, The role of elastin in the mechanical properties of skin, J. Biomech. 21 (3) (1988) 213–218, doi:10.1016/0021-9290(88)90172-8.

[10] H. Eshel, Y. Lanir, Effects of strain level and proteoglycan depletion on preconditioning and viscoelastic responses of rat dorsal skin, Ann. Biomed. Eng. 29 (2) (2001) 164–172, doi:10.1114/1.1349697.

[11] D. Veronda, R. Westmann, Mechanical characterization of skin—finite deformations, J. Biomech. 3 (1) (1970) 111–124, doi:10.1016/0021-9290(70)90055-2.

[12] I.A. Brown, A scanning electron microscope study of the effects of uniaxial tension on human skin, Br. J. Dermatol. 89 (4) (1973) 383–393, doi:10.1111/j.1365-2133.1973.tb02993.x.

[13] D.C. Schneider, T.M. Davidson, A.M. Nahum, In vitro biaxial stress-strain response of human skin, Arch. Otolaryngol. Head Neck Surg. 110 (5) (1984) 329–333, doi:10.1001/archotol.1984.00800310053012.

[14] K. Langer, On the anatomy and physiology of the skin. I. The cleavability of the cutis. (Translated from Langer, K. (1861). Zur Anatomie und Physiologie der Haut. I. Uber die Spaltbarkeit der Cutis. Sitzungsbericht der Mathematisch-naturwissenschaftlichen Classe der, Br. J. Plast. Surg. 31 (1) (1978) 3–8.

[15] C.H. Daly, G.F. Odland, Age-related changes in the mechanical properties of human skin, J. Invest. Dermatol. 73 (1) (1979) 84–87, doi:10.1111/1523-1747.ep12532770.

[16] A.B. Cua, K.P. Wilhelm, H.I. Maibach, Elastic properties of human skin: relation to age, sex, and anatomical region, Arch. Dermatol. Res. 282 (5) (1990) 283–288, doi:10.1007/BF00375720.

[17] B. Lynch, C. Bonod-Bidaud, G. Ducourthial, J.-S. Affagard, S. Bancelin, S. Psilodimitrakopoulos, F. Ruggiero, J.-M. Allain, M.-C. Schanne-Klein, How aging impacts skin biomechanics: a multiscale study in mice, Sci. Rep. 7 (1) (2017) 13750, doi:10.1038/s41598-017-13150-4.

[18] C.-Y. Lin, G.P. Sugerman, S. Kakaletsis, W.D. Meador, A.T. Buganza, M.K. Rausch, Sex- and age-dependent skin mechanics—A detailed look in mice, Acta Biomater. 175 (2024) 106–113, doi:10.1016/j.actbio.2023.11.032.

[19] M. Zhou, P.J. González, L. Van Haasterecht, A. Soylu, M. Mihailovski, P. Van Zuijlen, M.L. Groot, Uniaxial mechanical stretch properties correlated with three-dimensional microstructure of human dermal skin, Biomech. Model. Mechanobiol. (2024), doi:10.1007/s10237-023-01813-3.

[20] W. Shu, H. Heimark, N. Bertollo, D.J. Tobin, E.D. O'Cearbhaill, A.N. Annaidh, Insights into the mechanics of solid conical microneedle array insertion into skin using the finite element method, Acta Biomater. 135 (2021) 403–413, doi:10.1016/j.actbio.2021.08.045.

[21] V.D. Sree, A. Ardekani, P. Vlachos, A.B. Tepole, The biomechanics of autoinjector-skin interactions during dynamic needle insertion, J. Biomech. 134 (February) (2022) 110995, doi:10.1016/j.jbiomech.2022.110995.

[22] M. de Lucio, Y. Leng, H. Wang, A.M. Ardekani, P.P. Vlachos, G. Shi, H. Gomez, Computational modeling of the effect of skin pinch and stretch on subcutaneous injection of monoclonal antibodies using autoinjector devices, Biomech. Model. Mechanobiol. 22 (6) (2023) 1965–1982, doi:10.1007/s10237-023-01746-x.

[23] C. Stowers, T. Lee, I. Bilionis, A.K. Gosain, A.B. Tepole, Improving reconstructive surgery design using Gaussian process surrogates to capture material behavior uncertainty, J. Mech. Behav. Biomed.Mater. 118 (2021) 104340, doi:10.1016/j.jmbbm.2021.104340.

[24] A. Spagnoli, R. Alberini, E. Raposio, M. Terzano, Simulation and optimization of reconstructive surgery procedures on human skin, J. Mech. Behav. Biomed.Mater. 131 (2022) 105215, doi:10.1016/j.jmbbm.2022.105215.

[25] T.L.-W. Chen, D.W.-C. Wong, Y. Peng, M. Zhang, Prediction on the plantar fascia strain offload upon Fascia taping and Low-Dye taping during running, J. Orthop. Transl. 20 (2020) 113–121, doi:10.1016/j.jot.2019.06.006.

[26] Y. Liu, M. Pharr, G.A. Salvatore, Lab-on-skin: a review of flexible and stretchable electronics for wearable health monitoring, ACS Nano 11 (10) (2017) 9614–9635, doi:10.1021/acsnano.7b04898.

[27] K. Sun, H. Ko, H. Park, M. Seong, S. Lee, H. Yi, H.W. Park, T. Kim, C. Pang, H.E. Jeong, Hybrid architectures of heterogeneous carbon nanotube composite microstructures enable multiaxial strain perception with high sensitivity and ultrabroad sensing range, Small 14 (52) (2018), doi:10.1002/smll.201803411.

[28] S.-H. Heo, C. Kim, T.-S. Kim, H.-S. Park, Human-palm-inspired artificial skin material enhances operational functionality of hand manipulation, Adv. Funct. Mater. 30 (25) (2020), doi:10.1002/adfm.202002360.

[29] M. Kawai, M. Nie, H. Oda, Y. Morimoto, S. Takeuchi, Living skin on a robot, Matter 5 (7) (2022) 2190–2208, doi:10.1016/j.matt.2022.05.019. https://linkinghub.elsevier.com/retrieve/pii/S2590238522002399

[30] G.A. Holzapfel, J.A. Niestrawska, R.W. Ogden, A.J. Reinisch, A.J. Schriefl, Modelling non-symmetric collagen fibre dispersion in arterial walls, J. R. Soc. Interface 12 (106) (2015) 20150188, doi:10.1098/rsif.2015.0188.

[31] J.A. Niestrawska, C. Viertler, P. Regitnig, T.U. Cohnert, G. Sommer, G.A. Holzapfel, Microstructure and mechanics of healthy and aneurysmatic abdominal aortas: experimental analysis and modelling, J. R. Soc. Interface 13 (124) (2016) 20160620, doi:10.1098/rsif.2016.0620.

[32] S. Wang, H. Hatami-Marbini, Constitutive modeling of corneal tissue: influence of three-dimensional collagen fiber microstructure, J. Biomech. Eng. 143 (3) (2020) 031002, doi:10.1115/1.4048401.

[33] M.J. Sadeghinia, B. Skallerud, G.A. Holzapfel, V. Prot, Biomechanics of mitral valve leaflets: second harmonic generation microscopy, biaxial mechanical tests and tissue modeling, Acta Biomater. 141 (2022) 244–254, doi:10.1016/j.actbio.2022.01.003.

[34] K. Li, R.W. Ogden, G.A. Holzapfel, A discrete fibre dispersion method for excluding fibres under compression in the modelling of fibrous tissues, J. R. Soc. Interface 15 (138) (2018) 20170766, doi:10.1098/rsif.2017.0766.

[35] A.J. Schriefl, H. Wolinski, P. Regitnig, S.D. Kohlwein, G.A. Holzapfel, An automated approach for three-dimensional quantification of fibrillar structures in optically cleared soft biological tissues, J. R. Soc. Interface 10 (80) (2013) 20120760, doi:10.1098/rsif.2012.0760.

[36] S. Luebberding, N. Krueger, M. Kerscher, Mechanical properties of human skin in vivo : a comparative evaluation in 300 men and women, Skin Res. Technol. 20 (2) (2014) 127–135, doi:10.1111/srt.12094.

[37] J. Weickenmeier, M. Jabareen, E. Mazza, Suction based mechanical characterization of superficial facial soft tissues, J. Biomech. 48 (16) (2015) 4279–4286, doi:10.1016/j.jbiomech.2015.10.039.

[38] R.B. Groves, S.A. Coulman, J.C. Birchall, S.L. Evans, Quantifying the mechanical properties of human skin to optimise future microneedle device design, Comput. Methods Biomech. Biomed.Eng. 15 (1) (2012) 73–82, doi:10.1080/10255842.2011.596481.

[39] H. Wei, X. Liu, L. Li, C. Li, W. Chen, S. Wang, Z. Wang, J. Ma, Visual indentation apparatus and finite element modelling as a method to characterize 3D mechanical properties of facial skin in vivo, Mech. Mater. 157 (2021) 103852, doi:10.1016/j.mechmat.2021.103852.

[40] M.A. Kirby, P. Tang, H.-C. Liou, M. Kuriakose, J.J. Pitre, T.N. Pham, R.E. Ettinger, R.K. Wang, M. O'Donnell, I. Pelivanov, Probing elastic anisotropy of human skin in vivo with light using non-contact acoustic micro-tapping OCE and polarization sensitive OCT, Sci. Rep. 12 (1) (2022) 3963, doi:10.1038/s41598-022-07775-3.

[41] M. Nagle, S. Price, A. Trotta, M. Destrade, M. Fop, A. Ní Annaidh, Analysis of in vivo skin anisotropy using elastic wave measurements and Bayesian modelling, Ann. Biomed. Eng. 51 (8) (2023) 1781–1794, doi:10.1007/s10439-023-03185-2.

[42] D.W. Laurence, S. Wang, R. Xiao, J. Qian, A. Mir, H.M. Burkhart, G.A. Holzapfel, C.-H. Lee, An investigation of how specimen dimensions affect biaxial mechanical characterizations with CellScale BioTester and constitutive modeling of porcine tricuspid valve leaflets, J. Biomech. 160 (October) (2023) 111829, doi:10.1016/j.jbiomech.2023.111829.

[43] G.A. Holzapfel, R.W. Ogden, On planar biaxial tests for anisotropic nonlinearly elastic solids. A continuum mechanical framework, Math. Mech. Solids 14 (5) (2009) 474–489, doi:10.1177/1081286507084411.

[44] H. Fehervary, M. Smoljkić, J. Vander Sloten, N. Famaey, Planar biaxial testing of soft biological tissue using rakes: a critical analysis of protocol and fitting process, J. Mech. Behav. Biomed.Mater. 61 (2016) 135–151, doi:10.1016/j.jmbbm.2016.01.011.

[45] C. Laville, C. Pradille, Y. Tillier, Mechanical characterization and identification of material parameters of porcine aortic valve leaflets, J. Mech. Behav. Biomed.Mater. 112 (2020) 104036, doi:10.1016/j.jmbbm.2020.104036.
[46] A. Ní Annaidh, K. Bruyère, M. Destrade, M.D. Gilchrist, C. Maurini, M. Otténio, G. Saccomandi, Automated estimation of collagen fibre dispersion in the dermis and its contribution to the anisotropic behaviour of skin, Ann. Biomed. Eng. 40 (8) (2012) 1666–1678, doi:10.1007/s10439-012-0542-3.
[47] T.K. Tonge, L.M. Voo, T.D. Nguyen, Full-field bulge test for planar anisotropic tissues: Part II – A thin shell method for determining material parameters and comparison of two distributed fiber modeling approaches, Acta Biomater. 9 (4) (2013) 5926–5942, doi:10.1016/j.actbio.2012.11.034.
[48] M. Diab, N. Kumaraswamy, G.P. Reece, S.E. Hanson, M.C. Fingeret, M.K. Markey, K. Ravi-Chandar, Characterization of human female breast and abdominal skin elasticity using a bulge test, J. Mech. Behav. Biomed.Mater. 103 (2020) 103604, doi:10.1016/j.jmbbm.2019.103604.
[49] W.D. Meador, G.P. Sugerman, H.M. Story, A.W. Seifert, M.R. Bersi, A.B. Tepole, M.K. Rausch, The regional-dependent biaxial behavior of young and aged mouse skin: A detailed histomechanical characterization, residual strain analysis, and constitutive model, Acta Biomater. 101 (2020) 403–413, doi:10.1016/j.actbio.2019.10.020.
[50] K. Li, G.A. Holzapfel, Multiscale modeling of fiber recruitment and damage with a discrete fiber dispersion method, J. Mech. Phys. Solids 126 (2019) 226–244, doi:10.1016/j.jmps.2019.01.022.
[51] R. Alberini, A. Spagnoli, M.J. Sadeghinia, B. Skallerud, M. Terzano, G.A. Holzapfel, Fourier transform-based method for quantifying the three-dimensional orientation distribution of fibrous units, Sci. Rep. 14 (1) (2024) 1999, doi:10.1038/s41598-024-51550-5.
[52] J. Schindelin, I. Arganda-Carreras, E. Frise, V. Kaynig, M. Longair, T. Pietzsch, S. Preibisch, C. Rueden, S. Saalfeld, B. Schmid, J.-Y. Tinevez, D.J. White, V. Hartenstein, K. Eliceiri, P. Tomancak, A. Cardona, Fiji: an open-source platform for biological-image analysis, Nat. Methods 9 (7) (2012) 676–682, doi:10.1038/nmeth.2019.
[53] E. Fagerholt, T. Børvik, O. Hopperstad, Measuring discontinuous displacement fields in cracked specimens using digital image correlation with mesh adaptation and crack-path optimization, Opt. Lasers Eng. 51 (3) (2013) 299–310, doi:10.1016/j.optlaseng.2012.09.010.
[54] D. Sage, L. Donati, F. Soulez, D. Fortun, G. Schmit, A. Seitz, R. Guiet, C. Vonesch, M. Unser, DeconvolutionLab2: an open-source software for deconvolution microscopy, Methods 115 (2017) (2017) 28–41, doi:10.1016/j.ymeth.2016.12.015.
[55] S. Zhuo, X. Zhu, J. Chen, S. Xie, Quantitative biomarkers of human skin photoaging based on intrinsic second harmonic generation signal, Scanning 35 (4) (2013) 273–276, doi:10.1002/sca.21062.
[56] M.-T. Ke, S. Fujimoto, T. Imai, SeeDB: a simple and morphology-preserving optical clearing agent for neuronal circuit reconstruction, Nat. Neurosci. 16 (8) (2013) 1154–1161, doi:10.1038/nn.3447.
[57] D.S. Richardson, J.W. Lichtman, Clarifying tissue clearing, Cell 162 (2) (2015) 246–257, doi:10.1016/j.cell.2015.06.067.
[58] M.J. Sadeghinia, H.M. Aguilera, S. Urheim, R.M. Persson, V.S. Ellensen, R. Haaverstad, G.A. Holzapfel, B. Skallerud, V. Prot, Mechanical behavior and collagen structure of degenerative mitral valve leaflets and a finite element model of primary mitral regurgitation, Acta Biomater. 164 (2023) 269–281, doi:10.1016/j.actbio.2023.03.029.
[59] J.M. Bueno, R.M. Martinez-Ojeda, L.M. Mugnier, P. Artal, Deconvolution method for multiphoton microscopy: an application to thick ocular tissues, in: 2019 21st International Conference on Transparent Optical Networks (ICTON), IEEE, Angers, France, 2019, pp. 1–4, doi:10.1109/ICTON.2019.8840328.
[60] S.F. Gibson, F. Lanni, Experimental test of an analytical model of aberration in an oil-immersion objective lens used in three-dimensional light microscopy, J. Opt. Soc. Am. A 8 (10) (1991) 1601–1613, doi:10.1364/JOSAA.8.001601.
[61] H. Kirshner, D. Sage, M. Unser, 3D PSF models for fluorescence microscopy in ImageJ, in: Proceedings of the Twelfth International Conference on Methods and Applications of Fluorescence Spectroscopy, Imaging and Probes (MAF11), volume 1, 2011, p. 154. Strasbourg, French Republic
[62] A. Feuchtinger, A. Walch, M. Dobosz, Deep tissue imaging: a review from a preclinical cancer research perspective, Histochem. Cell Biol. 146 (6) (2016) 781–806, doi:10.1007/s00418-016-1495-7.
[63] M. Rolf-Pissarczyk, M.P. Wollner, D.R.Q. Pacheco, G.A. Holzapfel, Efficient computational modelling of smooth muscle orientation and function in the aorta, Proc. R. Soc. A Math.Phys. Eng. Sci. 477 (2255) (2021), doi:10.1098/rspa.2021.0592.
[64] G.A. Holzapfel, Nonlinear Solid Mechanics: A Continuum Approach for Engineering Science, Wiley, Chichester, 2000.
[65] M.S. Sacks, Biaxial mechanical evaluation of planar biological materials, J. Elast. 61 (2000) 199–246, doi:10.1023/A:1010917028671.
[66] C. Zaiontz, Real Statistics Using Excel, 2023, https://www.real-statistics.com.
[67] J. Murphy, W. Goodhall, A. Patterson, Langer's lines – what are they and do they matter? Br. J. Oral Maxillofac. Surg. 55 (10) (2017) e86–e87, doi:10.1016/j.bjoms.2017.08.012.
[68] M. Witte, S. Jaspers, H. Wenck, M. Rübhausen, F. Fischer, General method for classification of fiber families in fiber-reinforced materials: application to in-vivo human skin images, Sci. Rep. 10 (1) (2020) 10888, doi:10.1038/s41598-020-67632-z.
[69] S. Calve, A. Ready, C. Huppenbauer, R. Main, C.P. Neu, Optical clearing in dense connective tissues to visualize cellular connectivity in situ, PLOS ONE 10 (1) (2015) e0116662, doi:10.1371/journal.pone.0116662.
[70] M. Muntifering, D. Castranova, G.A. Gibson, E. Meyer, M. Kofron, A.M. Watson, Clearing for deep tissue imaging, Curr. Protoc. Cytometry 86 (1) (2018) 1–21, doi:10.1002/cpcy.38.
[71] S. Abadie, C. Jardet, J. Colombelli, B. Chaput, A. David, J. Grolleau, P. Bedos, V. Lobjois, P. Descargues, J. Rouquette, 3D imaging of cleared human skin biopsies using light-sheet microscopy: a new way to visualize in-depth skin structure, Skin Res. Technol. 24 (2) (2018) 294–303, doi:10.1111/srt.12429.
[72] Y. Tan, C.P.L. Chiam, Y. Zhang, H.L. Tey, L.G. Ng, Research techniques made simple: optical clearing and three-dimensional volumetric imaging of skin biopsies, J. Invest. Dermatol. 140 (7) (2020) 1305–1314.e1, doi:10.1016/j.jid.2020.04.014.
[73] S.W. Carmichael, The tangled web of Langer's lines, Clin. Anat. 27 (2) (2014) 162–168, doi:10.1002/ca.22278.
[74] A. Ní Annaidh, K. Bruyère, M. Destrade, M.D. Gilchrist, M. Otténio, Characterization of the anisotropic mechanical properties of excised human skin, J. Mech. Behav. Biomed.Mater. 5 (1) (2012) 139–148, doi:10.1016/j.jmbbm.2011.08.016.
[75] S.J. Mostafavi Yazdi, J. Baqersad, Mechanical modeling and characterization of human skin: a review, J. Biomech. 130 (2022) 110864, doi:10.1016/j.jbiomech.2021.110864.
[76] A.F. Borges, Relaxed skin tension lines (RSTL) versus other skin lines, Plast. Reconstr. Surg. 73 (1) (1984) 144–150, doi:10.1097/00006534-198401000-00036.
[77] G.A. Holzapfel, R.W. Ogden, On fiber dispersion models: exclusion of compressed fibers and spurious model comparisons, J. Elast. 129 (1–2) (2017) 49–68, doi:10.1007/s10659-016-9605-2.
[78] S. Budday, G. Sommer, C. Birkl, C. Langkammer, J. Haybaeck, J. Kohnert, M. Bauer, F. Paulsen, P. Steinmann, E. Kuhl, G. Holzapfel, Mechanical characterization of human brain tissue, Acta Biomater. 48 (2017) 319–340, doi:10.1016/j.actbio.2016.10.036.
[79] A.E. Ehret, K. Bircher, A. Stracuzzi, V. Marina, M. Zündel, E. Mazza, Inverse poroelasticity as a fundamental mechanism in biomechanics and mechanobiology, Nat. Commun. 8 (1) (2017) 1002, doi:10.1038/s41467-017-00801-3.
[80] A. Wahlsten, M. Pensalfini, A. Stracuzzi, G. Restivo, R. Hopf, E. Mazza, On the compressibility and poroelasticity of human and murine skin, Biomech. Model. Mechanobiol. 18 (4) (2019) 1079–1093, doi:10.1007/s10237-019-01129-1.
[81] P.D.H.M. Verhaegen, P.P.M. Van Zuijlen, N.M. Pennings, J. Van Marle, F.B. Niessen, C.M.A.M. Van Der Horst, E. Middelkoop, Differences in collagen architecture between keloid, hypertrophic scar, normotrophic scar, and normal skin: an objective histopathological analysis, Wound Repair Regen. 17 (5) (2009) 649–656, doi:10.1111/j.1524-475X.2009.00533.x.
[82] L. Mostaço-Guidolin, N. Rosin, T.-L. Hackett, Imaging collagen in scar tissue: developments in second harmonic generation microscopy for biomedical applications, Int. J. Mol. Sci. 18 (8) (2017) 1772, doi:10.3390/ijms18081772.
[83] L. Baumann, E.F. Bernstein, A.S. Weiss, D. Bates, S. Humphrey, M. Silberberg, R. Daniels, Clinical relevance of elastin in the structure and function of skin, Aesthetic Surg. J. Open Forum 3 (3) (2021) 1–8, doi:10.1093/asjof/ojab019.